Remote Sensing of Environment 236 (2020) 111480

Contents lists available at ScienceDirect

Remote Sensing of Environment

journal homepage: www.elsevier.com/locate/rse

# Monitoring the incidence of *Xylella fastidiosa* infection in olive orchards using ground-based evaluations, airborne imaging spectroscopy and Sentinel-2 time series through 3-D radiative transfer modelling

A. Hornero[a,*], R. Hernández-Clemente[a], P.R.J. North[a], P.S.A. Beck[b], D. Boscia[c], J.A. Navas-Cortes[d], P.J. Zarco-Tejada[b,d,e]

[a] Department of Geography, Swansea University, SA2 8PP, Swansea, United Kingdom
[b] European Commission (EC), Joint Research Centre (JRC), Directorate D-Sustainable Resources, Via E. Fermi 2749 – TP 261, 26a/043, I-21027, Ispra, VA, Italy
[c] CNR, Istituto per la Protezione Sostenibile delle Piante (IPSP), via Amendola, 122/D, I-70126, Bari, Italy
[d] Instituto de Agricultura Sostenible (IAS), Consejo Superior de Investigaciones Científicas (CSIC), Avenida Menéndez Pidal s/n, 14004, Córdoba, Spain
[e] School of Agriculture and Food, Faculty of Veterinary and Agricultural Sciences and Department of Infrastructure Engineering, Melbourne School of Engineering, University of Melbourne, Melbourne, Victoria, Australia

ARTICLE INFO

*Keywords:*
Sentinel-2
Hyperspectral
*Xylella fastidiosa*
Temporal change
Radiative transfer

ABSTRACT

Outbreaks of *Xylella fastidiosa* (*Xf*) in Europe generate considerable economic and environmental damage, and this plant pest continues to spread. Detecting and monitoring the spatio-temporal dynamics of the disease symptoms caused by *Xf* at a large scale is key to curtailing its expansion and mitigating its impacts. Here, we combined 3-D radiative transfer modelling (3D-RTM), which accounts for the seasonal background variations, with passive optical satellite data to assess the spatio-temporal dynamics of *Xf* infections in olive orchards. We developed a 3D-RTM approach to predict *Xf* infection incidence in olive orchards, integrating airborne hyperspectral imagery and freely available Sentinel-2 satellite data with radiative transfer modelling and field observations. Sentinel-2A time series data collected over a two-year period were used to assess the temporal trends in *Xf*-infected olive orchards in the Apulia region of southern Italy. Hyperspectral images spanning the same two-year period were used for validation, along with field surveys; their high resolution also enabled the extraction of soil spectrum variations required by the 3D-RTM to account for canopy background effect. Temporal changes were validated with more than 3000 trees from 16 orchards covering a range of disease severity (DS) and disease incidence (DI) levels. Among the wide range of structural and physiological vegetation indices evaluated from Sentinel-2 imagery, the temporal variation of the Atmospherically Resistant Vegetation Index (ARVI) and Optimized Soil-Adjusted Vegetation Index (OSAVI) showed superior performance for DS and DI estimation ($r^2_{VALUES} > 0.7$, $p < 0.001$). When seasonal understory changes were accounted for using modelling methods, the error of DI prediction was reduced 3-fold. Thus, we conclude that the retrieval of DI through model inversion and Sentinel-2 imagery can form the basis for operational vegetation damage monitoring worldwide. Our study highlight the value of interpreting temporal variations in model retrievals to detect anomalies in vegetation health.

## 1. Introduction

*Xylella fastidiosa* (*Xf*), a plant pathogenic bacterium that can live in the xylem of more than 300 plant species, causes severe damage to multiple crops around the world, including olive trees and stone fruits (Almeida and Nunney, 2015). The first outbreak of *Xf* in Europe was detected in olive orchards in Apulia (southern Italy) in 2013 (Saponari et al., 2017), and the pathogen has now been officially identified in France and Spain (EFSA, 2018) and very recently (2019) in Israel (EPPO, 2019). According to Saponari et al. (2017), olive stands can be infected for more than five months without visible symptoms. During this period, the bacterium can spread within the xylem tissue and, theoretically, cause water-related stress that may lead to, among other things, lower transpiration and photosynthetic rates. Symptoms then start to become visible, with a progressive increase in discolouration and defoliation of the tree crowns within a few months, leading to tree

* Corresponding author.
*E-mail address:* alberto.hornero@swansea.ac.uk (A. Hornero).

https://doi.org/10.1016/j.rse.2019.111480
Received 14 March 2019; Received in revised form 21 September 2019; Accepted 16 October 2019
Available online 18 November 2019
0034-4257/ 

death within a few years.

Accurate detection and diagnosis of *Xf* symptoms is critical for the operational monitoring of *Xf* spread and for the reduction of losses in crop yield (Sisterson et al., 2010). Recent work showed that early symptoms of *Xf* infection in olive trees are detectable through very high-resolution hyperspectral and thermal remote sensing images acquired from airborne platforms: these symptoms manifest as alterations in photoprotective mechanisms, reduction in photosynthetic activity due to photosynthetic pigment reduction and degradation processes, and decreased chlorophyll fluorescence emission and plant transpiration rates (Zarco-Tejada et al., 2018a). Unfortunately, while airborne imaging spectroscopy permits the detection of early and even non-visible symptoms of *Xf* infection, such tree-level alterations cannot be detected directly by current satellite sensors due to their limited spectral and spatial resolutions. However, we hypothesise that symptoms at intermediate to advanced stages of *Xf* disease, which are visible as leaf browning, wilting, chlorosis, and desiccation of leaves, should be observable in Sentinel-2 satellite data due in large part to the spectral bands located in the red-edge region, which is sensitive to photosynthetic pigment absorption. Satellite-based monitoring of such symptoms could support the monitoring of *Xf* spread over large areas, providing the spatial distribution related to the epidemiology of *Xf* and contributing to the assessment of vegetation health by environmental managers and other end-users. Furthermore, the short revisit interval (up to every 2–3 days) of this satellite at moderate latitudes provides key temporal information about short-term variation in vegetation status over large areas.

Sentinel-2 images from 2015 on are freely available and combine moderate-to-high spatial resolution (10 to 60 m) in 13 spectral bands, with a revisit time of five days. Given their combination of spatial, spectral, and temporal resolution, Sentinel-2 data could, in theory, be used to help monitor the spread of *Xf* over entire regions with a frequency not achievable by other means. Pre-launch studies using simulated Sentinel-2 data products demonstrated the potential of the sensor to measure biophysical variables such as chlorophyll content (William James Frampton et al., 2013) and leaf area index (Herrmann et al., 2011). The added value of the Sentinel-2's red-edge bands consists of increased accuracies for the estimation of chlorophyll content (Zarco-Tejada et al., 2019), the fractional cover (FC) of forest canopies, the quantification of leaf area index (LAI) (Korhonen et al., 2011), and land-cover mapping (Forkuor et al., 2018). Sentinel-2 data thus widen the possibility of using passive optical satellite data for vegetation monitoring, particularly in non-homogeneous and complex canopies (Lange et al., 2017). The temporal resolution of Sentinel-2 can report trends in vegetation characteristics affected by infective agents with higher accuracy than other satellites such as Landsat (Rahimzadeh-Bajgiran et al., 2018) or MODIS (Mura et al., 2018). Recent studies have investigated the actual capabilities of the sensor for monitoring temporal changes in vegetation activity in canopy types such as wetlands (Araya-López et al., 2018; Whyte et al., 2018), grasslands (Hill, 2013) and forests (Castillo et al., 2017; Zarco-Tejada et al., 2018b). To the extent of our knowledge, no prior studies have explored the applicability of Sentinel-2 to evaluation of the spectral variations produced by *Xf*-induced disease.

Despite the widespread interest in Sentinel-2, its spatial resolution causes mixed-pixel effects that make it challenging when attempting to separate the contribution of the different canopy-scene components such as soil, shadows, and understory, particularly in open vegetation canopies. This aspect is critical in the case of olive orchards, where planting densities are typically in the range of 200 to 2000 trees/ha and the canopy is rarely closed (Sibbett and Ferguson, 2005). The mixture of canopy-scene components hampers the scaling up of plant functional traits from views of pure tree crowns to broader spatial scales. Furthermore, the understory and soil in these landscapes vary spatially and seasonally as a result of vegetation phenology, agricultural practices, and soil–vegetation understory dynamics, impacting the multi-temporal spectral datasets.

Common approaches to assessing vegetation traits from passive optical satellite observations include the use of vegetation indices (VIs) and radiative transfer models (RTMs). The Normalized Difference Vegetation Index (NDVI) has been widely applied for vegetation trend analysis (Beck et al., 2011; Fang et al., 2018; Gillespie et al., 2018) and to monitor vegetation productivity in olive groves (Brilli et al., 2013; Noori and Panda, 2016). In addition to its strengths, the limitations of NDVI for vegetation monitoring have received much attention in the literature (Montandon, 2009; Myneni et al., 1991); these limitations stem from its sensitivity to soil and atmospheric features, and its tendency to saturate in high-biomass environments. Potential alternatives include the Soil-Adjusted Vegetation Index (SAVI) (Huete, 1988), Adjusted Transformed Soil-Adjusted Vegetation Index (ATSAVI) (Baret and Guyot, 1991), atmospherically resistant vegetation index (ARVI) (Huete et al., 1994) and Global Environment Monitoring Index (GEMI) (Pinty and Verstraete, 1992). For instance, ARVI has a similar dynamic range to NDVI, but on average it has been demonstrated to be four times less sensitive to atmospheric effects compared to NDVI (Kaufman and Tanre, 1992a). However, the spectral mixture obtained with medium-resolution satellite observations inherently limits the extent to which VIs can scale up field observations of plant functional traits to entire landscapes (Atzberger and Richter, 2012; Zurita-Milla et al., 2015). In addition, the large contributions to the spectral reflectance of the canopy produced by variation in the understory could have important implications for the applicability of VIs to temporal change analysis. The literature lacks studies focused on the sensitivity of VIs to variations in both vegetation health and temporal change, including the contribution of changes in the understory that heavily affect the reflectance acquired by Sentinel-2 images.

RTMs can overcome some of these typical limitations of purely empirical approaches, minimising the dependence on field measurements and modelling the reflectance mixture produced by the contribution of different components at medium resolutions. These two factors are essential to improving the retrieval of biophysical vegetation parameters over time. For uniform canopies, 1-D RTMs such as SAIL (Verhoef, 1984) have been successfully used to monitor grass and crop stress (Bayat et al., 2016; Martín et al., 2007). However, modelling heterogeneous and discontinuous vegetation canopies requires complex 3-D RTM models that account for tree canopy structure and background effects. Previous studies have used FLIGHT to provide a 3-D representation of tree canopies and perform the spatial and spectral scaling of different biophysical variables (Bye et al., 2017; Hernández-Clemente et al., 2017). Still, none of these models includes the effects produced by the understory on the spectral reflectance in open canopies. The variations in understory are especially important in natural environments, with high impacts on time-series data analysis over heterogeneous and sparse canopies (Assal et al., 2016; Yang et al., 2014). Other RTMs such as DART (Gastellu-Etchegorry et al., 1996) have overcome these limitations and could particularly benefit the simulation of the canopy. By contrast, the large number of parameters needed in complex 3-D models limits the inversion procedures (Hernández-Clemente et al., 2014; Yáñez-Rausell et al., 2015).

Here, we investigate the suitability of Sentinel-2 satellite images for monitoring disease symptoms in *Xf*-infected olive orchards. Using field observations and multi-temporal remote sensing data, we assessed (i) the capability of physiological and structural VIs calculated from Sentinel-2 imagery to accurately evaluate DI and DS in olive orchards infected by *Xf* in southern Italy, and (ii) whether the application of a 3-D radiative transfer model to account for temporal changes in the soil and understory improves the prediction of *Xf*-disease incidence from Sentinel-2 time-series data.


**Fig. 1.** Sentinel 2A scene of southern Italy (large inset, A) with an overlay (green box, B) in which airborne hyperspectral mosaics are shown. The three hyperspectral images were acquired from aircraft on 28 June 2016 with a micro-hyperspectral imager (red box, C) yielding 40-cm spatial resolution. The infected zone highlighted in the main map (A) outlines the area where *Xylella fastidiosa* has been observed as of March 2018 (Commission Implementing Decision (EU) 2018/927, 2018). (For interpretation of the references to colour in this figure legend, the reader is referred to the Web version of this article.)

## 2. Materials and methods

### 2.1. Study site and field data collection

The study was conducted in an olive-growing area (*Olea europaea* L.) in Apulia (southern Italy, 40°30′50″N, 18°01′50″E) where *Xf* was officially detected for the first time in October 2013 (Fig. 1). The phytosanitary measures implemented have been unsuccessful in preventing the spread of *Xf* throughout southern Apulia. The area is characterised by a temperate climate with mild winters and a landscape dominated by olive orchards that favour the natural spread of *Xf* (Saponari et al., 2017; Strona et al., 2017). By 2015, the pathogen had spread to ca. 275,000 ha in the region, and it currently affects an area greater than 600,000 ha (labelled as 'Infected zone' in Fig. 1A).

Field surveys were carried out in 16 olive orchards located in the *Xf*-infected zone in which qPCR analysis had confirmed its presence (Zarco-Tejada et al., 2018a). During the surveys, disease severity (DS) and disease incidence (DI) were assessed for 3300 olive trees. Seem (1984) defines DS as the quantity of disease that is affecting entities within a sampling unit; DI is a quantal measure, defined as the proportion or percentage of diseased entities within a sampling unit. DS thus accounts for disease severity, while DI only considers whether a tree is affected or not. DI is, therefore, quicker and easier to measure, and generally more accurate and reproducible than other quantitative measures, making it the commonly preferred measurement method for the detection and enumeration of disease propagation patterns (Horsfall and Cowling, 1978). Based on visual inspection, we assigned individual trees to one of the five DS categories available (Fig. 2) depending on the proportion of the crown affected by typical *Xf* symptoms including desiccation and discolouration of leaves and branches. DS ranged from 0, indicating the absence of symptoms, to 4, when most of the branches in the crown were dead (Table 1). DI was either 0 or 1, indicating non-symptomatic trees and symptomatic trees, respectively, where non-symptomatic trees corresponded to a DS of 0 and symptomatic trees to any other severity (DS > 0; Fig. 2. From these assessments for each tree, we calculated the average DS and DI of all trees for each orchard (DSo and DIo, respectively).

The first field survey was conducted in June 2016 and observed 48.5% of the trees to be asymptomatic; when the survey was repeated in July 2017, this value was 15.2%. Symptomatic trees were identified in all sampled orchards in both years, with a minimum DIo of 25.0% and 63.9% in 2016 and 2017, respectively. These values reflect the fact that all of the olive orchards across a very large region, extending more than 50 km from our study sites, are infected to some degree (Fig. 1). Given the ubiquity of *Xf* in such area and the challenge of locating an area free of *Xf*, a direct comparison between *Xf*-infected and *Xf*-free

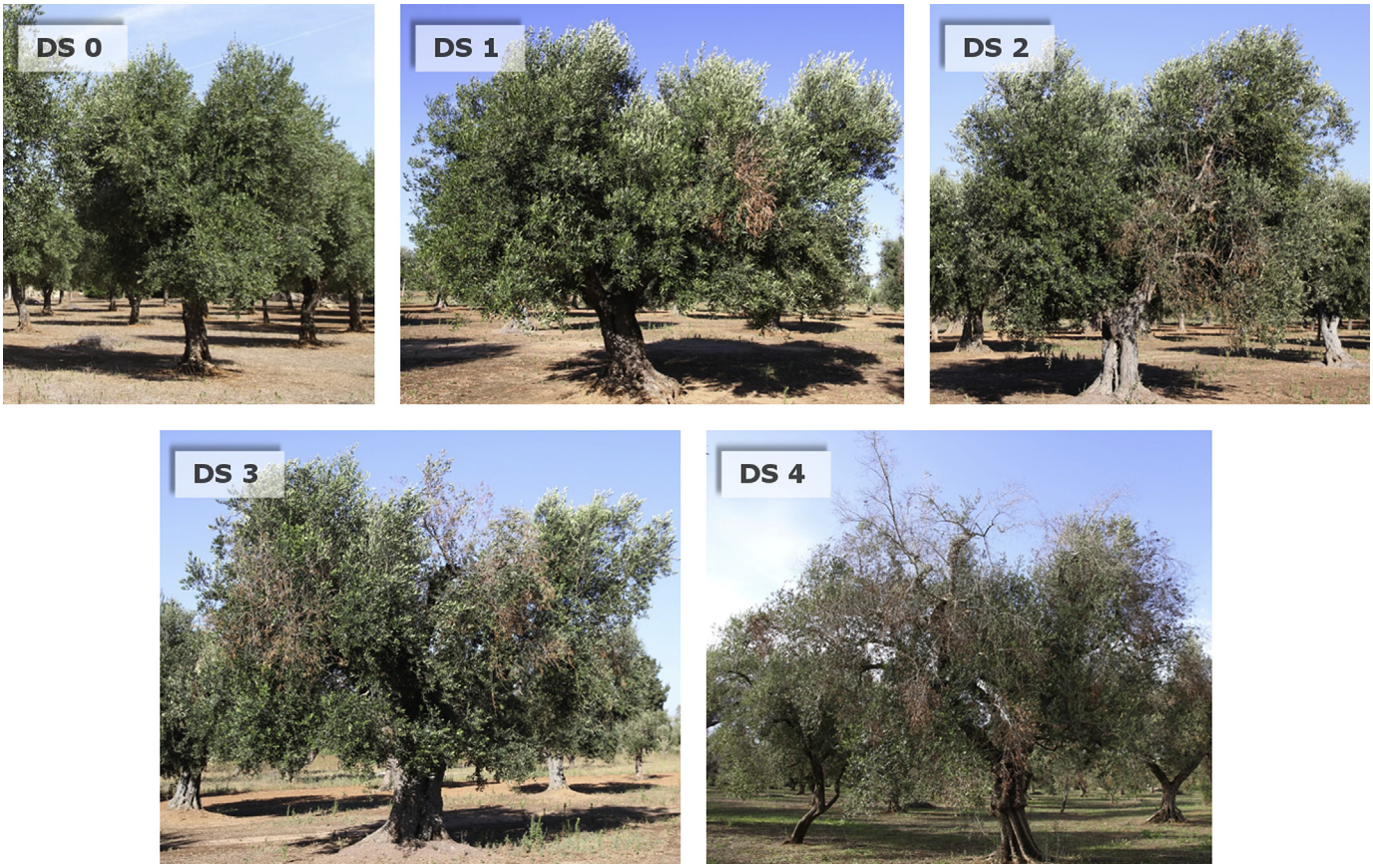


**Fig. 2.** Examples of the five disease severity (DS) classes that olive trees (n = 3300) were assigned to during a field survey in 2016 that was repeated in 2017. The classes related to the extent of severity of typical visual symptoms of *Xylella fastidiosa* ranging from apparently healthy trees (DS = 0) to trees showing canopies with a prevalence of dead branches (DS = 4).

orchards experiencing similar environmental conditions was not possible. The relative increase of *Xf* infection in the surveyed orchards, expressed as ΔDS and ΔDI, was measured based on the DSo and DIo observed between the 2016 and 2017 field surveys as:

$$\Delta DS = (DSo_{year\ n+1} - DSo_{year\ n})/DSo_{year\ n} \quad (1)$$

$$\Delta DI = (DIo_{year\ n+1} - DIo_{year\ n})/DIo_{year\ n} \quad (2)$$

where values above zero for ΔDS and ΔDI imply an aggravation of the visual symptoms, zero values correspond to orchards with no significant changes, and values below zero indicate a lessening of visual symptoms in an orchard.

### 2.2. Sentinel-2a imagery

A temporal dataset of Sentinel-2 images was used to analyse the feasibility of detecting the ΔDS and ΔDI of *Xf* infection using VI trends. The Multispectral Instrument (MSI), on board Sentinel-2A, acquires imagery at a 10-day interval under constant viewing conditions, which results in 4- to 6-day revisit times at mid-latitudes due to the swath overlap between neighbouring orbits. The MSI measures reflected radiance in 13 spectral bands from visible and near-infrared (VNIR) to short-wave infrared (SWIR), with images at 12 bits per channel and a spatial resolution of 10 m (Central Wavelength [CWL] at 496.6, 560.0, 664.5 and 835.1 nm with a bandwidth of 98, 45, 38 and 145 nm, respectively), 20 m (CWL at 703.9, 740.2, 782.5, 864.8, 1613.7 and 2202.4 nm with a bandwidth of 19, 18, 28, 33, 143 and 242 nm, respectively) and 60 m (CWL at 443.9, 945.0 and 1373.5 nm with a bandwidth of 27, 26 and 75 nm, respectively).

We used the multi-temporal Sentinel-2A data available for the first two complete years after its launch in 2015 to build a multi-temporal spectral dataset from the 86 cloud-free Sentinel-2A images (Level-1C, ortho-rectified imagery expressed in top-of-atmosphere reflectance) (Richter et al., 2011) available from July 2015 to August 2017. From Level-1C, the images were atmospherically corrected to generate Level-2A (bottom-of-atmosphere – surface reflectance – provided with a pixel classification mask) with Sen2Cor (version 2.3.1). Using the scene

**Table 1**
*Xylella fastidiosa* evaluation criteria: crown-level severity and incidence assignment.

| DS Level | Severity | Description | Desiccation | Incidence |
|---|---|---|---|---|
| 0 | Healthy | Symptomless | 0% | No incidence |
| 1 | Initial severity | Few desiccated branches affecting a limited part of the canopy | > 0 ≤ 25% | Incidence |
| 2 | Medium severity | Desiccation affecting a large part of the canopy | > 25 ≤ 50% | Incidence |
| 3 | High severity | Canopy with desiccated branches uniformly distributed | > 50 ≤ 75% | Incidence |
| 4 | Very high severity | Severe tree decline | > 75% | Incidence |

**Table 2**
Vegetation indices derived from Sentinel-2 data included in this study and their formulations.

| Vegetation index | Equation | Reference |
|---|---|---|
| *Normalized Difference Vegetation Index* | $NDVI = (R_{800} - R_{670})/(R_{800} + R_{670})$ | Rouse et al. (1974) |
| *Chlorophyll Index* | $CI = \frac{R_{750}}{R_{710}}$ | Zarco-Tejada et al. (2001) |
| *Normalized Difference Index* | $NDI = (R_{706} - R_{664})/(R_{704} + R_{664})$ | Delegido et al. (2011) |
| *MERIS Terrestrial Chlorophyll Index* | $MTCI = (R_{754} - R_{709})/(R_{709} - R_{681})$ | Dash and Curran (2007) |
| *Modified Chlorophyll Absorption Ratio Index* | $MCARI = ((R_{700} - R_{670}) - 0.2(R_{700} - R_{550}))\left(\frac{R_{700}}{R_{670}}\right)$ | Haboudane et al. (2004) |
| *Green Normalized Difference Vegetation Index* | $GNDVI = (R_{800} - R_{550})/(R_{800} + R_{550})$ | Gitelson et al. (1996) |
| *Pigment Specific Simple Ratio A* | $PSSRa = \frac{R_{800}}{R_{680}}$ | Blackburn (1998) |
| *Sentinel-2 Red-Edge Position* | $S2REP = 705 + 35\frac{\frac{R_{783}+R_{665}}{2} - R_{705}}{R_{740} - R_{705}}$ | W. J. Frampton et al. (2013) |
| *Inverted Red-Edge Chlorophyll Index* | $IRECI = (R_{783} - R_{665})/(R_{705} + R_{740})$ | W. J. Frampton et al. (2013) |
| *Renormalized Difference Vegetation Index* | $RDVI = (R_{800} - R_{670})/\sqrt{(R_{800} + R_{670})}$ | Roujean and Breon (1995) |
| *Modified Simple Ratio* | $MSR = \frac{R_{800}/R_{670} - 1}{(R_{800}/R_{670})^{0.5} + 1}$ | Chen (1996) |
| *Transformed Chlorophyll Absorption Ratio* | $TCARI = 3\left((R_{700} - R_{670}) - 0.2(R_{700} - R_{550})\frac{R_{700}}{R_{670}}\right)$ | Haboudane et al. (2002) |
| *Optimized Soil-Adjusted Vegetation Index* | $OSAVI = (1 + 0.16)\frac{R_{800} - R_{670}}{R_{800} + R_{670} + 0.16}$ | Rondeaux et al. (1996) |
| *Modified Soil-Adjusted Vegetation Index* | $MSAVI = (1 + L)\frac{R_{800} - R_{670}}{R_{800} + R_{670} + L}$ | Qi et al. (1994) |
| *TCARI/OSAVI* | $TCARI/OSAVI = \frac{\text{TCARI}}{\text{OSAVI}}$ | Haboudane et al. (2002) |
| *Modified Chlorophyll Absorption Ratio Index 1510* | $MCARI1510 = ((R_{700} - R_{1510}) - 0.2(R_{700} - R_{550}))\left(\frac{R_{700}}{R_{1510}}\right)$ | Herrmann et al. (2010) |
| *Transformed Chlorophyll Absorption Ratio 1510* | $TCARI1510 = 3\left((R_{700} - R_{1510}) - 0.2(R_{700} - R_{550})\frac{R_{700}}{R_{1510}}\right)$ | Herrmann et al. (2010) |
| *Optimized Soil-Adjusted Vegetation Index 1510* | $OSAVI1510 = (1 + 0.16)\frac{R_{800} - R_{1510}}{R_{800} + R_{1510} + 0.16}$ | Herrmann et al. (2010) |
| *Red Green Ratio Index* | $IRG = R_{670} - R_{550}$ | Gamon and Surfus (1999) |
| *Perpendicular Vegetation Index* | $PVI = \frac{R_{800} - a \cdot R_{670} - b}{\sqrt{a^2 + 1}}$ | Richardson and Wiegand (1977) |
| *Ratio Vegetation Index - Simple Ratio 800/670* | $RVI = \frac{R_{800}}{R_{670}}$ | Pearson and Miller (1972) |
| *Adjusted Transformed Soil-Adjusted VI* | $ATSAVI = a \cdot \frac{R_{800} - a \cdot R_{670} - b}{a \cdot R_{800} + R_{670} - ab + x(1 + a^2)}$ | Baret and Guyot (1991) |
| *Atmospherically Resistant Vegetation Index* | $ARVI = \frac{R_{800} - R_{670} - y(R_{670} - R_{450})}{R_{800} + R_{670} - y(R_{670} - R_{450})}$ | Bannari et al. (1995) |
| *Global Environment Monitoring Index* | $GEMI = n(1 - 0.25n)\frac{R_{670} - 0.125}{1 - R_{670}}$ <br> $n = \frac{2(R_{800}^2 - R_{670}^2) + 1.5 \cdot R_{800} + 0.5 \cdot R_{670}}{R_{800} + R_{670} + 0.5}$ | Pinty and Verstraete (1992) |
| *Difference Vegetation Index* | $DVI = g \cdot R_{800} - R_{670}$ | Richardson and Wiegand (1977) |
| *Aerosol Free Vegetation Index 1600* | $AFRI1510 = R_{800} - 0.66\frac{R_{1600}}{R_{800} + 0.66 \cdot R_{1600}}$ | Karnieli et al. (2001) |
| *Aerosol Free Vegetation Index 2100* | $AFRI2100 = R_{800} - 0.5\frac{R_{2100}}{R_{800} + 0.56 \cdot R_{2100}}$ | Karnieli et al. (2001) |

classification from Level-2A, we then filtered the data that were affected by clouds or cirrus before calculating a suite of VIs.

We selected spectral VIs that are primarily sensitive to canopy structure or pigment concentration and compatible with the spectral bandset of Sentinel-2. The equations and references for each VI are shown in Table 2. More precisely, we calculated (i) conventional and corrected ratio and normalized indices derived from the near-infrared and red bands such as the Normalized Difference Vegetation Index (NDVI), Modified Simple Ratio (MSR), Green Normalized Difference Vegetation Index (GNDVI) and Renormalized Difference Vegetation Index (RDVI); (ii) conventional soil-adjusted indices such as the Adjusted Transformed Soil-Adjusted VI (ATSAVI), Optimized Soil-Adjusted Vegetation Index (OSAVI) and Modified Soil-Adjusted Vegetation Index (MSAVI), and corrected versions using SWIR bands such as $OSAVI_{1510}$; (iii) conventional and corrected chlorophyll VIs such as the Chlorophyll Index (CI), Normalized Difference Index (NDI), Medium Resolution Imaging Spectrometer (MERIS) Terrestrial Chlorophyll Index (MTCI), Pigment Specific Simple Ratio A (PSSRa), Sentinel-2 Red-Edge Position (S2REP), and Inverted Red-Edge Chlorophyll Index (IRECI); and (iv) chlorophyll indices formulated to minimise their sensitivity to structural effects based on the Chlorophyll Absorption in Reflectance Index (CARI) and its transformations into Transformed Chlorophyll Absorption Ratio Index (TCARI) and Modified Chlorophyll Absorption Ratio Index (MCARI) normalized by OSAVI in the form $^{\text{TCARI}}/_{\text{OSAVI}}$ and $MCARI_{1510}$ using SWIR bands, as formulated in Table 2. Finally, a smoothing algorithm based on Local Polynomial Regression Fitting (Cleveland et al., 1992) was used to reduce atmospheric variability and fill gaps to produce daily time series of the indices.

For each of the 16 orchards, we used the daily dataset of VIs to calculate the values for June 2016 and July 2017, taking the means over 2-week intervals centred on the dates of the ground measurement collection to reduce random fluctuations in time-series data. We additionally calculated the temporal rate of change for each VI in the form $VI_{year=n+1}/VI_{year=n}$ in order to understand the temporal trajectory of VIs as a function of *Xf* infection. Finally, Pearson correlation analysis and p-values, adjusted with a Bonferroni correction to control false

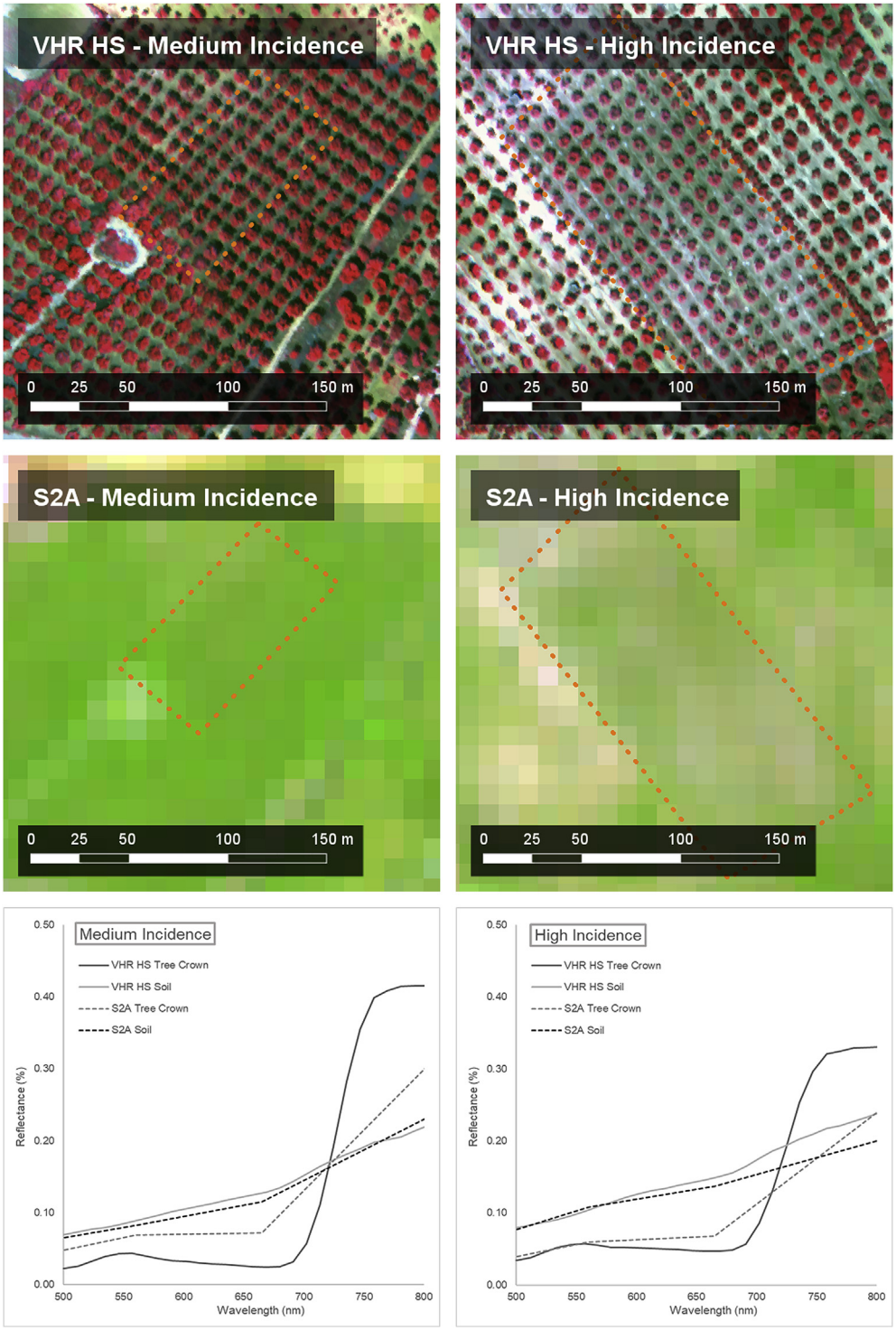


**Fig. 3.** Example of olive orchards with medium (left panels) and high (right panels) incidence of *Xf*-related disease, viewed by an airborne high-resolution narrow-band hyperspectral camera (VHR HS, top row), by Sentinel-2A (S2A, middle row, RGB-composite of bands B3, B2 and B4) and through their spectral signatures captured by the VHR HS and S2A (bottom row).

positives (Haynes, 2013), were used to determine the strength and statistical significance of the relationship between the in-situ measurements of *Xf* impact, i.e. ΔDI and ΔDS, and the rate of change of VIs derived from Sentinel-2 data.

### 2.3. Airborne hyperspectral images

For validation purposes, we collected very high-resolution images (Fig. 3) on 28th June 2016 and 3rd July 2017 using a micro-hyperspectral imager—Micro-Hyperspec VNIR model (Headwall Photonics Inc., Fitchburg, MA, USA)—on board a Cessna aircraft. Visible and near-infrared spectral regions (400–885 nm) were covered by operating the sensor with 260 bands and a radiometric resolution of 12 bits at a 1.865 nm CWL interval, yielding 6.4 nm full-width at half-maximum (FWHM) spectral resolution with a 25-μm slit. The acquisition frame-rate on board the aircraft was 50 frames per second with an integration

time of 18 ms; with a focal length of 8 mm, an angular field of view (FOV) of 49.82° was produced (corresponding to an instantaneous FOV [IFOV] of 0.93 mrad). More platform and sensor configuration details can be found in Zarco-Tejada et al. (2013). The hyperspectral sensor was radiometrically calibrated in the laboratory with an integrating sphere (CSTM-USS-2000C Uniform Source System from Labsphere, North Sutton, NH, USA) by calculating coefficients derived from the calibrated light source at four illumination levels. The atmospheric correction was carried out using the total incoming irradiance simulated with the SMARTS model (Gueymard, 1995, 2001), which allowed the conversion of radiance values to reflectance. The model was fed with data from a weather station (WX510 from Vaisala, Vantaa, Finland) and a Microtops II Sunphotometer (Solar Light Co., Philadelphia, PA, USA). Hyperspectral imagery was ortho-rectified with PARGE (ReSe Applications Schläpfer, Wil, Switzerland) using inputs from an inertial measurement unit (MTiG from Xsens, Enschede, Netherlands) installed on board and synchronized with the imager; image correction and data pre-processing are described in detail in Hernández-Clemente et al. (2012) and Zarco-Tejada et al. (2016).

The hyperspectral images had a ground resolution of 40 cm, allowing us to distinguish individual olive tree crowns from the background made up of soil and understory vegetation. We used the hyperspectral images to evaluate the contribution of the background to the relationship between ΔDI and the rate of change of VIs derived from the Sentinel-2 data. To do this, we calculated for each orchard the hyperspectral VIs separately for the background areas surrounding the trees – by defining each tree crown as the area within a 5-m radius from the centroid and then masking the crowns by image segmentation – and for the tree crowns only.

We also used the very high-resolution images as ground-truth for model parametrisation, detailed in the next section, following the methodology proposed by Zarco-Tejada et al. (2019) using scene components extracted from airborne hyperspectral images. Fig. 4 shows a strong correlation between VIs derived from Sentinel-2 and hyperspectral images over the 16 olive orchards in both 2016 ($r^2 = 0.86$, $p < 0.001$ for NDVI and $r^2 = 0.78$, $p < 0.001$ for OSAVI) and 2017 ($r^2 = 0.68$, $p < 0.001$ for NDVI and $r^2 = 0.66$, $p < 0.001$ for OSAVI). The consistency between the two datasets enabled the use of the high-resolution imagery as ground-truth for model parametrisation (Fig. 4).

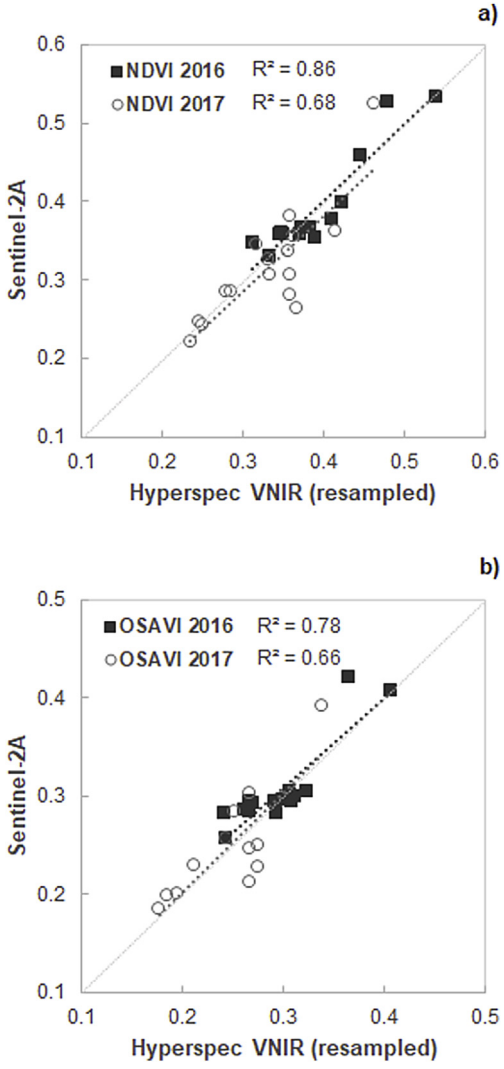


**Fig. 4.** Comparison between Sentinel-2A and high-spatial-resolution aircraft (Hyperspec VNIR) imagery using the vegetation indices NDVI (a) and OSAVI (b) of 16 olive orchards surveyed in June 2016 and July 2017.

### 2.4. Model simulations

We used a coupled leaf-canopy radiative transfer model to analyse the sensitivity of different VIs to orchard-level changes in *Xf*-induced disease incidence through time and to evaluate the effects of the background and soil on symptom detection. The leaf optical properties were simulated with the PROSPECT-D model (Feret et al., 2017), which requires seven variables: the leaf structure coefficient (N), chlorophyll content ($C_{a+b}$), carotenoid content ($C_{x+c}$), anthocyanin content (Anth), brown pigment content ($C_{brown}$), water equivalent thickness ($C_w$) and dry matter content ($C_m$). The PROSPECT leaf model was coupled to the 3-dimensional FLIGHT model (Hernández-Clemente et al., 2017; North, 1996) to simulate the optical effects stemming from heterogeneous architecture of the olive tree crowns and orchards. FLIGHT uses Monte Carlo Ray Tracing (MCRT) techniques to simulate the radiative transfer within and between tree crowns and other canopy components. FLIGHT calculates directional reflectance of the canopy by accumulating photon energy in the observation direction as a function of different components defining the canopy structure (crown shape and size, tree height, position, density and distribution) (Table 3).

Using the described PROSPECT + FLIGHT modelling approach, we generated a lookup table (LUT) to investigate the temporal dynamics of *Xf*-induced disease incidence using VIs calculated from simulated spectra. We built a LUT with 7056 simulations using the input parameters described in Table 3. The nominal values used to generate the simulations were defined based on field measurements and hyperspectral imagery (Table 3) to mimic the orchards' architecture and the level of disease impact across the study area. The 40-cm spatial resolution hyperspectral images (Fig. 3 top) were used to distinguish the scene components (Fig. 5), facilitating the parametrisation of the FLIGHT model simulations. In particular, we quantified the fractional cover of each orchard (FCo) using NDVI calculated from the high-resolution hyperspectral image. A threshold of NDVI > 0.3 was applied to distinguish tree crowns from background pixels during image segmentation according to Niblack's thresholding method (Niblack, 1986) and Sauvola's binarization techniques (Sauvola and Pietikäinen, 2000). Next, we applied a binary watershed analysis using the Euclidean distance map for each object to automatically separate trees with overlapping crowns, which enables one to rebuild the scene with the same features. The FCo values retrieved from the airborne sensor were related to the field observations (DSo and DIo), with a linear regression model ($r^2 = 0.67$, $p < 0.05$) used as a proxy for DSo and DIo in the model simulation. The relationship between FCo and DSo was used to mimic the natural range of variation in FCo values for each DSo and used as input in the LUT. The initial LUT was then classified to set an approximate range of FCo per DSo and DIo (Table 4). For each class (DSo Level 0 to 4), we assumed a range of crown diameters and LAI per orchard to comply with the FCo defined for each level. We also assumed a decrease in the chlorophyll content values corresponding to the

**Table 3**
Nominal values used in PROSPECT + FLIGHT simulation analysis.

| Variable | Variable code | Nominal values |
|---|---|---|
| *PROSPECT* | | |
| *Structure coefficient* | N | 1.2 |
| *Chlorophyll a+b content* | $C_{a+b}$ (μg/cm$^2$) | 10–80 |
| *Carotenoid content* | $C_{x+c}$ (μg/cm$^2$) | 10 |
| *Anthocyanin content* | Anth (μg/cm$^2$) | 1.0 |
| *Brown pigment content* | $C_{brown}$ (arb. unit) | 0.0 |
| *Water content* | $C_w$ (cm) | 0.015 |
| *Dry matter* | $C_m$ (g/cm$^2$) | 0.009 |
| *FLIGHT* | | |
| *Mode of operation* | MODE | r (reverse) |
| *Dimension of model* | FLAG | 3 (3D Representation) |
| *Solar zenith, view zenith (°)* | θs, θv | 39.27, 0.0 |
| *Solar azimuth, view azimuth (°)* | Φs, Φv | 103.87, 0.0 |
| *Number of wavebands* | NO_WVBANDS | 401 |
| *Image size* | IM_SIZE | 200 x 200 |
| *Number of photons traced* | – | 40000 (reverse mode, from image size) |
| *Total LAI (LAI crown)* | TOTAL_LAI | 0.25–3.5 |
| *Leaf angle distribution* | LAD [1–9] | 0.015, 0.045, 0.074, 0.1,0.123, 0.143, 0.158, 0.168, 0.174 |
| *Fractional cover (%)* | FRAC_COV | 5–55 |

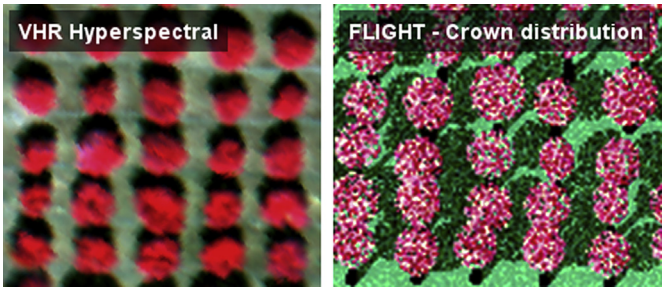


**Fig. 5.** Overview of an olive grove acquired with a 40-cm hyperspectral sensor enabling the identification of single trees (left panel) and a 3-D scene generated with FLIGHT Monte Carlo simulation mimicking crown distribution (right panel).

**Table 4**
Classification criteria in the model inversion, including disease severity (DSo) and fractional cover (FCo) at orchard level, leaf area index at both crown ($LAI_{CROWN}$) and scene level ($LAI_{SCENE}$), and chlorophyll content ($C_{a+b}$).

| DSo Level | Description | FCo (%) | $LAI_{CROWN}$ | $C_{a+b}$ | $LAI_{SCENE}$ |
|---|---|---|---|---|---|
| 0 | Healthy | 45–55 | 2–3.5 | 65–80 | 0.9–1.925 |
| 1 | Initial severity | 25–45 | 1.5–2 | 50–65 | 0.375–0.9 |
| 2 | Medium severity | 20–25 | 0.75–1.5 | 35–50 | 0.15–0.375 |
| 3 | High severity | 10–20 | 0.5–0.75 | 20–35 | 0.05–0.15 |
| 4 | Very high severity | 5–10 | 0.25–0.5 | 10–20 | 0.0125–0.05 |

increase in DSo to mimic the typical discolouration observed in *Xf*-infected olive trees.

To define the synthetic dataset associated with the change, we established a pool of combinations of change describing the positive increase rate of severity ($c = \sum_{k=1}^{5} k$) between orchards classified at different levels for the years $n$ and $n+1$ (*year* $n_{L4}$→ *year* $n+1_{L4}$, *year* $n_{L3}$→ *year* $n+1_{L3}$, *year* $n_{L3}$→ *year* $n+1_{L4}$, …, *year* $n_{L0}$→ *year* $n+1_{L4}$). The rate of change between simulations for years $n$ and $n+1$ was used for the final retrieval of ΔDI and ΔDS.

Three different approaches were evaluated to account for the canopy background in the simulations: (i) a more complex solution that included the background spectral reflectance variation recorded by the hyperspectral images between 2016 and 2017 for each plot, named here as the "temporal background per plot" (TBP); (ii) a simpler approach considering a "persistent spectral reflectance for the background" (PB) using a bare-soil spectrum extracted from the hyperspectral imagery collected in 2016; and (iii) a compromise alternative that computed the average of the background's spectral reflectance recorded for all plots during 2016 and 2017, named here as the "mean temporal background scheme" (MTB). The performance of the model under each strategy was evaluated based on the Root Mean Square Error (RMSE) between the DI increase estimated from the retrieved Sentinel-2 data and the field-observed DI scored for each of the 16 orchards evaluated.

## 3. Results

In this section we present results from empirical approaches to detect variations in DI of *Xf*-infected olive orchards using physiological and structural VIs calculated from Sentinel-2 imagery. Then, we report results using a 3-D radiative transfer model to predict temporal changes of *Xf*-induced disease incidence that accounts for the soil and understory variations affecting the temporal trends.

### 3.1. Temporal trends of DS and DI and vegetation indices

Both DI and DS caused by *Xf* increased between 2016 and 2017 in all of the surveyed olive orchards (Fig. 6). DS and DI were significantly correlated with each other ($r^2 = 0.84$, $p < 0.05$), as were the temporal change rates ΔDS and ΔDI ($r^2 = 0.79$, $p < 0.05$). Orchards where incidence had already reached 100% in 2016 continued to see an increase in symptom severity (e.g. Fig. 6, orchards A5 and A4), and orchards with a low initial incidence and severity (e.g. C20 to B3), showed a strong increase in both one year later, as reflected by high ΔDI and ΔDS, respectively.

The rate of change in 17 out of the 26 Sentinel-2 VIs correlated

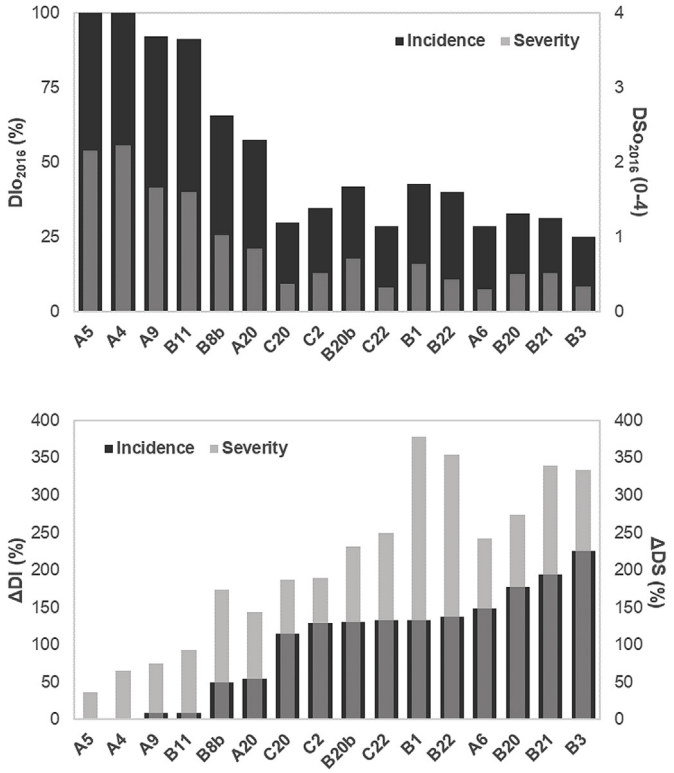


**Fig. 6.** Temporal evolution of DIo and DSo between 2016 and 2017. (Top) DS and DI in 2016; (bottom) ΔDI and ΔDS between 2016 and 2017. X-axis labels refer to the 16 olive orchards surveyed.

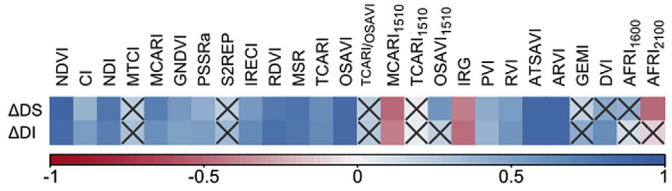


**Fig. 7.** Relationship between increases in severity (ΔDS) and incidence (ΔDI) and temporal rate of change in Sentinel-2 vegetation indices selected for this study. Correlation coefficients range from −1 to 1. Cross (X) symbols indicate non-significant relationships (p-value ≥ 0.001).

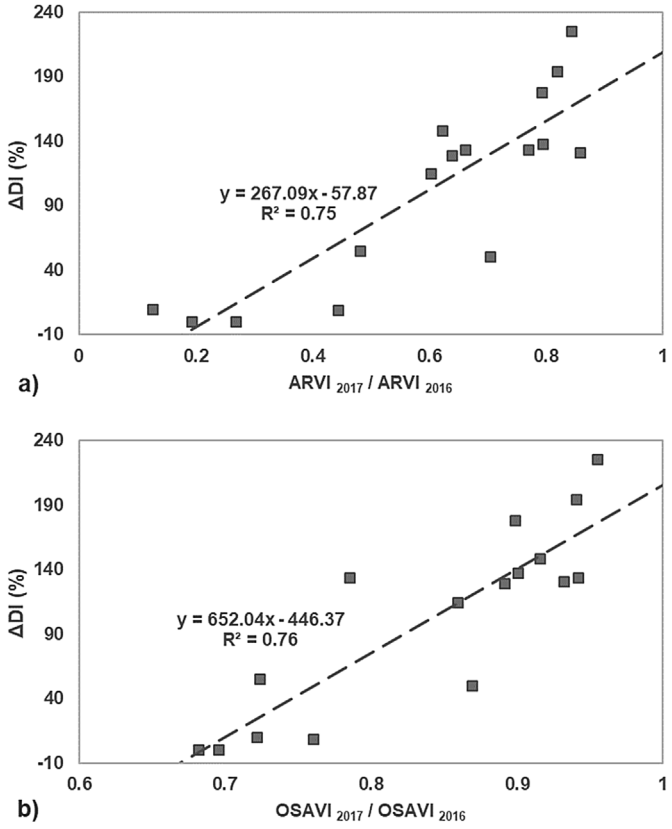


**Fig. 8.** Relationship between *Xf* incidence increase (ΔDI) and the rate of change of the vegetation indices ARVI (a) and OSAVI (b). Rate of change was calculated from Sentinel-2 images taken in 2016 and 2017.

significantly ($p < 0.001$) with both ΔDS and ΔDI, and six of them showed a coefficient of determination ($r^2$) exceeding 0.57 (Fig. 7). The indices ARVI and OSAVI produced the highest coefficients of determination with ΔDI ($r^2 = 0.75$ and $r^2 = 0.76$, respectively; $p < 0.001$) (Fig. 8). Other VIs such as ATSAVI and NDVI yielded similar results ($r^2 = 0.72$ and $r^2 = 0.71$, respectively), outperforming RDVI ($r^2 = 0.65$) and MSR ($r^2 = 0.61$). The relationships between these VIs and ΔDS yielded similar results ($r^2_{ARVI} = 0.74$, $r^2_{OSAVI} = 0.71$, $r^2_{ATSAVI} = 0.72$, $r^2_{NDVI} = 0.71$, $r^2_{RDVI} = 0.57$, $r^2_{MSR} = 0.6$; $p < 0.001$ in all cases). Surprisingly, however, greater ΔDI values were associated with smaller reductions in the VIs (Fig. 8), whether considering entire orchards (Fig. 8), the background cover only (Fig. 9a), or tree crowns only (Fig. 9b). Furthermore, VIs calculated from the background area around each tree, made up of soil and understory vegetation and excluding tree crowns, displayed a similar pattern in which orchards with greater ΔDI showed smaller VI reductions (Fig. 9).

The analysis of the temporal changes observed by Sentinel-2A ARVI and OSAVI revealed distinct patterns in orchards with medium and high DI over the last two years (Fig. 10). Orchards with high DI had a lower

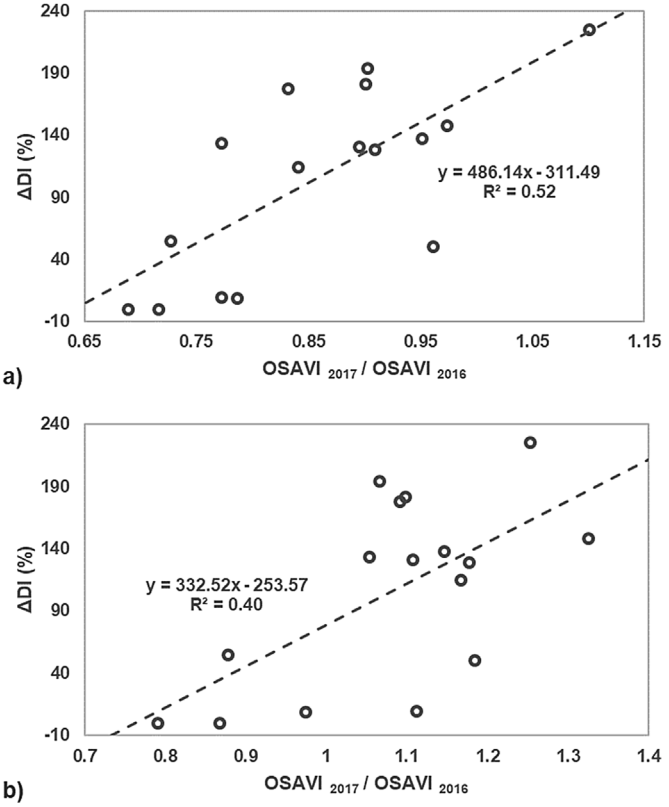


**Fig. 9.** Relationship between *Xf* incidence increase (ΔDI) and the rate of change of the vegetation index OSAVI with the background around a tree, determined by assuming a radius of 5 m around the centroid of each tree and masking the tree crowns by segmentation (a); and taking only tree crowns (b). Rate of change was calculated from hyperspectral imagery in 2016 and 2017 due to its resolution sufficient to discriminate between background and trees.

ARVI and OSAVI than those with medium DI. The differences between medium and high DI were more substantial during the summer, when the VIs tended to be lower than in winter, and much less variable than in spring, when infection symptoms develop more rapidly and potentially depend on local-scale environmental conditions as well as on the physiological status of individual trees.

### 3.2. Modelling changes in vegetation trends with Sentinel-2

The results of the radiative transfer modelling approach, which was proposed to evaluate the sensitivity of VIs to track the temporal evolution of *Xf* disease, are displayed in Fig. 11. The FLIGHT model simulations obtained using a synthetic multi-temporal dataset, built with inputs within the typical range of variation observed in olive groves affected by *Xf* in two consecutive years for OSAVI (Fig. 11a) and ARVI (Fig. 11b), showed a direct relationship between ΔDI and the rate of change between two consecutive years. The simulated VIs generated using the MTB approach were significantly related to ΔDI for OSAVI, ARVI and NDVI, and yielded similar accuracy to the empirical relationship with OSAVI ($r^2 = 0.74$) but somewhat lower accuracy with ARVI ($r^2 = 0.49$) and higher with NDVI ($r^2 = 0.68$) (data not shown). In any case, the linear responses of the simulated VIs matched the empirical relationships very closely.

ΔDI estimated through model inversion using two different VIs (ARVI and OSAVI) corresponded well with the field observations of the ΔDI temporal change (Fig. 12). The complexity in accounting for the background in the models had an effect on the goodness-of-fit, introducing a bias in the DI change estimates (Fig. 12); when the year-to-year evolution of the background was considered independently for

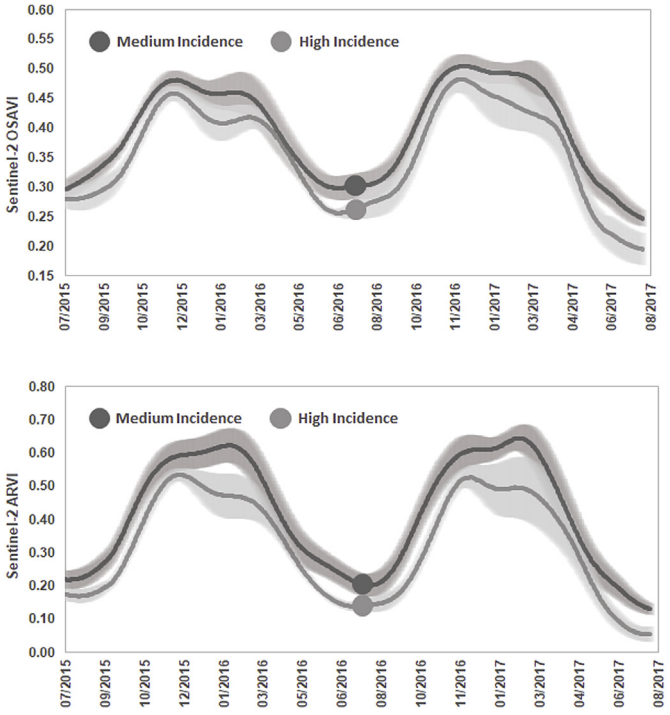


**Fig. 10.** Daily mean OSAVI (top) and ARVI (bottom) two-year time series of orchards with medium and high *Xf* incidence as evaluated in the field on 28 June 2016 (dots indicate the timing of the field survey). Lines represent the mean of medium-incidence ($DIo_{2016}$ < 50%; n = 10) and high-incidence ($DIo_{2016}$ > 50%; n = 6) orchards, and bands extend two standard deviations around them.

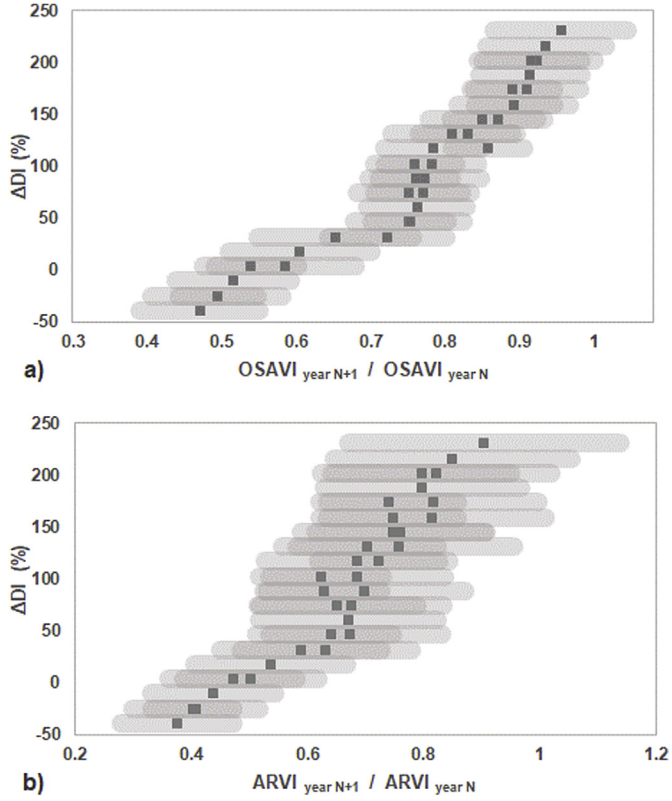


**Fig. 11.** Simulations of the disease incidence increase (ΔDI) with OSAVI (a) and ARVI (b), generated by PROSPECT + FLIGHT and using the average spectral reflectance measured in parts of the orchards not covered by olive tree crowns to represent the background in the model (MTB approach). Bands surrounding the points show the variability in results for the same ΔDI, and the points themselves are the average values within those simulations.

each of the orchards (TBP approach), the model simulations were entirely corrected for background effects and, therefore, the accuracy of ΔDI retrievals using OSAVI and ARVI was significantly higher ($RMSE_{OSAVI}$ = 43% and $RMSE_{ARVI}$ = 44%; $NRMSE_{OSAVI}$ = 0.19 and $NRMSE_{ARVI}$ = 0.20) (Fig. 12a, b). Model performance decreased when instead the mean background reflectance time series from all orchards (MTB approach) was used as a model input ($RMSE_{OSAVI}$ = 50% and $RMSE_{ARVI}$ = 84%; $NRMSE_{OSAVI}$ = 0.22 and $NRMSE_{ARVI}$ = 0.36) (Fig. 12c, d). Finally, when model simulations did not account for the temporal changes in background reflectance at all (PB approach), the fitted models degraded significantly, leading to even larger errors (RMSE ≥ 140%; NRMSE > 0.6) (Fig. 12e, f).

Applying model-inversion methodology with OSAVI and the MTB model (Figs. 11a and 12c) to entire Sentinel-2A scenes generated a map of the predicted yearly increase in *Xf*-induced disease incidence between June 2016 and 2017 (Fig. 13). Looking in detail at four of the surveyed olive orchards (bottom panels in Fig. 13), representing a range of predicted ΔDI values, we can confirm that predictions of low to high percentages (0 to 180%) of *Xf*-disease incidence increase corresponded with the field observation records, which reported ΔDI from 0 to 194% for those fields. Furthermore, predicted maps generated with the model show enough spatial resolution to provide operational monitoring at the orchard level.

## 4. Discussion

The first research aim of this study was to determine whether satellite data could be used to monitor temporal changes of *Xf*-induced DI and DS, and to provide insights into the epidemiology of *Xf* spread over large areas. Non-visual symptoms of *Xf* infection can be detected using very high-resolution hyperspectral images and radiative transfer models (Zarco-Tejada et al., 2018a), providing an innovative tool for the early detection of infected olive trees on a local scale. However, since *Xf* has spread rapidly in southern Italy over the last few years, affecting entire olive orchards, tracking more conspicuous damage (such as DI and DS) across large areas could help measure, forecast, and mitigate the impact of *Xf* on the landscape and on socio-economic sectors depending on it (Luvisi et al., 2017; White et al., 2017). The fast spread of *Xf* was reflected in our field observations: DI and DS increased considerably between 2016 and 2017, and ΔDI and ΔDS were linearly related. Indeed, the widespread increase of *Xf* infections in the last three years in southern Apulia (Girelli et al., 2017) has posed a risk to the olive trees and to this economic sector in the region.

Under natural conditions, biotic and abiotic factors jointly affect the development of vegetation diseases over different spatial and temporal scales. The interaction may cause a progressive loss in chlorophyll and biomass, producing irreversible changes in the vegetation. Both alterations are detectable and quantifiable through VIs calculated from Sentinel-2 data (Zarco-Tejada et al., 2019). However, the relationships between VIs (OSAVI or NDVI) and DS or DI were poor when considering data from 2016 and 2017 together ($r^2$ < 0.22, p < 0.05) (Fig. S1, supplementary material), indicating that the VIs reflect orchard characteristics other than *Xf* symptoms and that such characteristics vary considerably between years. Hence, a precise disease assessment requires a quantitative estimation of the temporal evolution of the disease (ΔDI and ΔDS) rather than a mere quantification of DI and DS at one specific time (Nutter et al., 2006). Indeed, the availability of frequent multispectral data from Sentinel-2 offers the opportunity to assess both spatial and temporal variation in VIs to monitor *Xf* infections in olive orchards over time.

When working with multi-temporal data acquired over non-closed canopies, one of the main challenges is to decouple the spectral reflectance changes produced by alterations in the vegetation condition

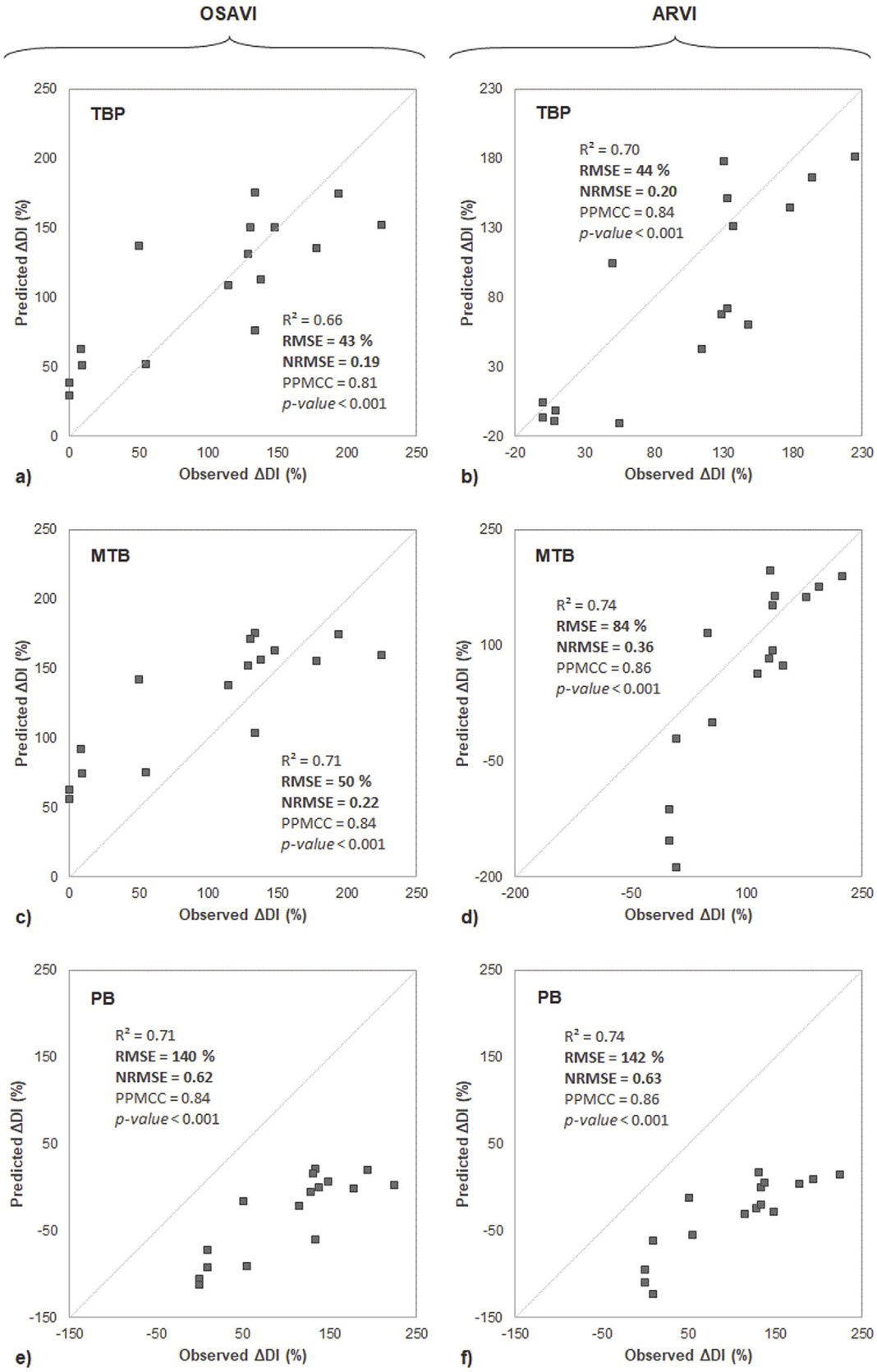


**Fig. 12.** Estimated versus measured *Xf* incidence increase (ΔDI) using OSAVI (left) and ARVI (right) vegetation indices. Graphs show PROSPECT + FLIGHT inversions calculated using TBP (a, b), MTB (c, d) and PB (e, f); see text for details.

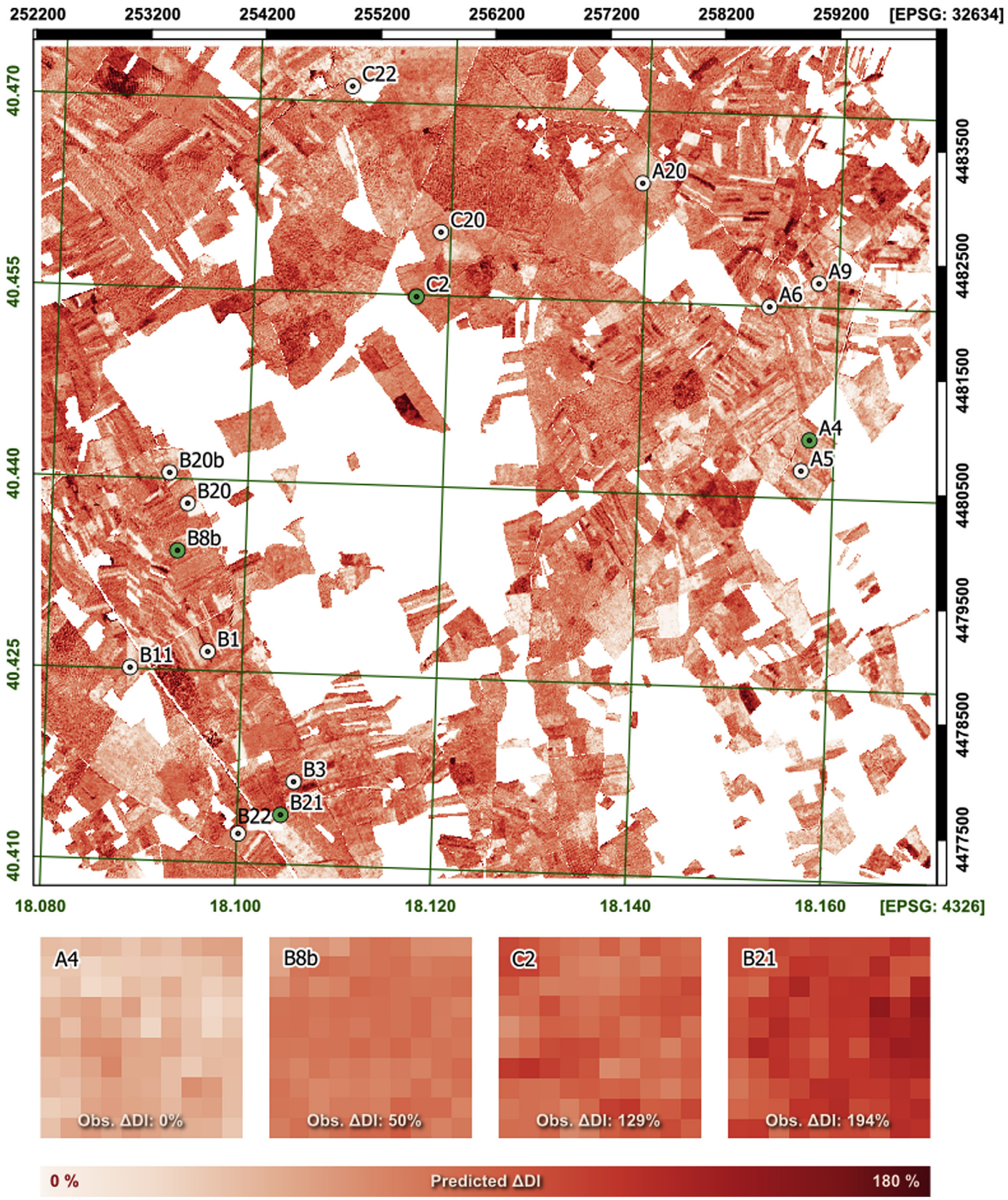


**Fig. 13.** *Xf*-disease incidence increase (ΔDI) map generated from Sentinel-2A data of 29th June 2016 and 24th June 2017 using a lookup table (LUT) generated by inverting a PROSPECT + FLIGHT model that considered the temporal changes in background reflectance across all orchards (MTB approach; see text for details). Dots in the map indicate the individual olive orchards that were surveyed in the field. Bottom panels show incidence increases over different areas (green dots) where olive orchards were surveyed, representing a range of predicted ΔDI values. The observed incidence increase for each selected orchard is also indicated. The map has been masked with a layer of olive groves for Puglia extracted from the Puglia Land Cover 2011 (InnovaPuglia Spa - Servizio Territorio e Ambiente, 2013). (For interpretation of the references to colour in this figure legend, the reader is referred to the Web version of this article.)

from those produced by atmospheric and background factors. Here, the seasonal variation of VIs showed the highest variability in winter and early spring. In these periods, cloudy days are more frequent, increasing the residual noise in the data and the need for temporal interpolation. The sensitivity of different VIs to soil background and atmospheric effects were previously analysed in efforts to improve the accuracy of the retrieval of LAI and absorbed photosynthetically active radiation (APAR) (Baret and Guyot, 1991; Haboudane et al., 2004; Huete et al., 1985) and chlorophyll (Haboudane et al., 2008; Zhang et al., 2008). The variation in FC of a forest under decline also affects the performance of some VIs with higher sensitivity to canopy structure changes (Hernández-Clemente et al., 2011). The best-performing VIs in our study, OSAVI and ARVI, tend to be relatively robust to background and atmospheric effects (Kaufman and Tanre, 1992b; Rondeaux et al., 1996). Empirical and modelling results agreed regarding the accuracy of OSAVI as the best-performing index to track ΔDI. By contrast, the performance of ARVI with regard to the field observations was not entirely confirmed by model simulations. This may be related to the fact that ARVI is a vegetation index that minimises the atmospheric effects on the reflectance, conditions that were not included in the modelling, which assumed stable conditions for both years.

The overall robustness shown by modified VIs such as OSAVI or ARVI is in disagreement with some other studies, in which traditional indices yielded better performance. For instance, Frampton et al. (2013) reported that LAI and chlorophyll could be extracted from Sentinel-2 NDVI images for crops as well as from novel indices such as S2REP and MTCI. Differences in the homogeneity of crop versus olive orchard canopies might explain this apparent contradiction: in the latter case, the confounding effects produced by the structural heterogeneity of the orchards invalidated VIs with high sensitivity to soil effects and atmospheric conditions.

The contribution of the background seems to affect not only the spectral reflectance of the canopy measured by Sentinel-2 but also the spectral reflectance retrieved from the diseased crowns using hyperspectral images. Both sensors, with different spatial and spectral resolutions, showed a significant and similar relationship, with greater ΔDI leading to smaller VI reductions. This counterintuitive result is unlikely to be driven by weather patterns in the two years, as the sampled orchards experienced very similar meteorological conditions. Instead, it might reflect the impact of the background on the crown spectral response because olive tree crowns generally display low crown transmittance and LAI (Gσmez Calero et al., 2011), and defoliation increases with DS. As a result, the background has a particularly large contribution to temporal VI trends once the *Xf* disease symptoms increase, even when using self-corrected (Kaufman and Tanre, 1992b) and soil-adjusted (Rondeaux et al., 1996) VIs and considering only tree crowns. Simultaneously, the increase in *Xf* infection was associated with a decrease in FC of the trees and an increase in the FC of the background, further increasing the dominance of the understory in the signal at orchard-level resolution. This inverse effect, i.e. an increase in the greenness of the background when the health of *Xf*-infected trees decreases, could be due to orchard management if diseased orchards are abandoned and no longer mowed or ploughed, leaving low-stature vegetation to reoccupy the soil. It may also be partly ecologically driven if diseased trees leave more nutrients and water available to the understory (Peltzer and Köchy, 2001).

This pattern further emphasises the relevance of incorporating 3-D RTMs when analysing VIs to explicitly incorporate background effects if the impact of *Xf* on spectral characteristics of olive groves is to be modelled with considerable precision (Meggio et al., 2008; Richardson and Wiegand, 1977). This conclusion links to our second research question, which focused on the feasibility of modelling changes in DI from multi-temporal Sentinel-2 image data using VIs and radiative transfer models. In fact, the background effect has a significant impact on the model estimation against in-situ measurements: there was an improvement in the retrieval of ΔDI of 33.5% when accounting for the background effects, and a further 9.5% improvement when its heterogeneity was also considered. These results have critical implications in the use of VIs to assess the temporal evolution of the disease due to the non-homogeneous background effects across orchards affected by *Xf*, which alter the spectral signature of the canopy obtained with Sentinel-2 image data. The simulation approach demonstrated the benefit of using a 3-D radiative transfer model accounting for such effects, which is critical when monitoring the future spread of *Xf* infections and understanding its epidemiology (Fuente et al., 2018). Therefore, this study takes one step further via modelling methods to properly account for the changes observed in canopy monitoring studies, enabling the retrieval of vegetation trends associated with *Xf* infections and improving the understanding of the dynamics of the understory.

The proposed methodology based on the use of RTM and Sentinel-2 imagery offers the advantage of using free satellite data over any other remote sensing product limited by the availability of hyperspectral images. However, the applicability of these methods within a systematic detection system may be limited by the computational time required for model inversion, notwithstanding this limitation can be overcome in combination with data-driven machine learning algorithms based on multi-output methods emulating the functioning of RTM (Rivera et al., 2015). The result of mapping disease-incidence dynamics using radiative transfer modelling illustrates the potential of the Sentinel-2 sensor to assess olive groves' health dynamics. The challenge of mapping disease infections has been thus far mainly addressed using environmental data and probabilistic models (Hay et al., 2006) and rarely approached in quantitative terms. Remote sensing that combines physical methods and VIs makes it possible to map the DI dynamics of *Xf* based on the main biophysical changes it causes at the landscape scale. The dense time series provided by Sentinel-2 satellites make continuous mapping feasible and bring new opportunities for monitoring diseases incidence worldwide. Future work should consider methods to disentangle direct plant-level effects of *Xf* infection from those that manifest themselves in other components of the landscape because of changes in either vegetation composition or management.

## 5. Conclusions

This study demonstrates that Sentinel-2 data enables the detection of changes associated with temporal variations of *Xf*-induced symptoms at the orchard level. The use of satellite imagery to monitoring large-scale dynamics is key to combat *Xf* infections. Our work took advantage of a two-year dataset collected in the *Xf*-infected area in southern Italy, integrating Sentinel-2 satellite images and high-resolution hyperspectral imagery, field observations and radiative transfer modelling. The temporal rate of change of disease incidence (DI) and disease severity (DS) was evaluated using different VIs and showed that the monitoring of *Xf*-infected orchards required the use of self-corrected and soil-adjusted VIs. Among the Sentinel-2 VI assessments, the best performance was observed for those that minimised the atmospheric and background effects such as ARVI, OSAVI and ATSAVI. These VIs performed better than traditional VIs such as NDVI, RDVI and MSR. However, the confounding effects of the understory had a considerable impact on the VIs obtained from Sentinel-2 over *Xf*-infected olive orchards due to the discontinuous canopy that characterises this crop. This study demonstrated that 3-D RTM and field observations properly explained the temporal variations experienced by both the tree canopy and the background, a critical aspect to accurately predicting ΔDI and ΔDS. Applying a temporal trend analysis supported by the 3-D RTM demonstrated that ARVI and OSAVI can be used to monitor orchard-level changes in DI and DS, yielding Normalized Root Mean Square Error (NRMSE) values below 0.22 and 0.36, respectively, for the two years of analysis. Overall, these results suggest that Sentinel-2 time-series imagery can provide useful spatio-temporal indicators to monitor the damage caused by *Xf* infections across large areas.

## Acknowledgements

Data collection was partially supported by the European Union's Horizon 2020 research and innovation programme through grant agreements POnTE (635646) and XF-ACTORS (727987). A. Hornero was supported by research fellowship DTC GEO 29 “Detection of global photosynthesis and forest health from space” from the Science Doctoral Training Centre (Swansea University, UK). The authors would also like to thank QuantaLab-IAS-CSIC (Spain) for laboratory assistance and the support provided during the airborne campaigns and image processing. B. Landa, C. Camino, M. Montes-Borrego, M. Morelli, M. Saponari and L. Susca are acknowledged for their support during the field campaigns, as well as IPSP-CNR and Dipartimento di Scienze del Suolo (Università di Bari, Italy) as host institutions. The views expressed are purely those of the writers and may not in any circumstance be regarded as stating an official position of the European Commission.

All the figures included in this manuscript have been designed by taking into account colour schemes prepared for people with visual disabilities and ensuring that they can be printed correctly (Harrower and Brewer, 2003).

## Appendix A. Supplementary data

Supplementary data to this article can be found online at https://doi.org/10.1016/j.rse.2019.111480.

## References

Almeida, R.P.P., Nunney, L., 2015. How do plant diseases caused by Xylella fastidiosa emerge? Plant Dis. 99, 1457–1467. https://doi.org/10.1094/PDIS-02-15-0159-FE.

Araya-López, R.A., Lopatin, J., Fassnacht, F.E., Hernández, H.J., 2018. Monitoring Andean high altitude wetlands in central Chile with seasonal optical data: a comparison between Worldview-2 and Sentinel-2 imagery. ISPRS J. Photogrammetry Remote Sens. 145, 213–224. https://doi.org/10.1016/j.isprsjprs.2018.04.001.

Assal, T.J., Anderson, P.J., Sibold, J., 2016. Spatial and temporal trends of drought effects in a heterogeneous semi-arid forest ecosystem. For. Ecol. Manag. 365, 137–151. https://doi.org/10.1016/j.foreco.2016.01.017.

Atzberger, C., Richter, K., 2012. Spatially constrained inversion of radiative transfer models for improved LAI mapping from future Sentinel-2 imagery. Remote Sensing of Environment, The Sentinel Missions - New Opportunities for Science 120, 208–218. https://doi.org/10.1016/j.rse.2011.10.035.

Bannari, A., Morin, D., Bonn, F., Huete, A.R., 1995. A review of vegetation indices. Remote Sens. Rev. 13, 95–120. https://doi.org/10.1080/02757259509532298.

Baret, F., Guyot, G., 1991. Potentials and limits of vegetation indices for LAI and APAR assessment. Remote Sens. Environ. 35, 161–173. https://doi.org/10.1016/0034-4257(91)90009-U.

Bayat, B., Van der Tol, C., Verhoef, W., 2016. Remote sensing of grass response to drought stress using spectroscopic techniques and canopy reflectance model inversion. Remote Sens. 8, 557. https://doi.org/10.3390/rs8070557.

Beck, P.S.A., Juday, G.P., Alix, C., Barber, V.A., Winslow, S.E., Sousa, E.E., Heiser, P., Herriges, J.D., Goetz, S.J., 2011. Changes in forest productivity across Alaska consistent with biome shift. Ecol. Lett. 14, 373–379. https://doi.org/10.1111/j.1461-0248.2011.01598.x.

Blackburn, G.A., 1998. Spectral indices for estimating photosynthetic pigment concentrations: a test using senescent tree leaves. Int. J. Remote Sens. 19, 657–675. https://doi.org/10.1080/014311698215919.

Brilli, L., Chiesi, M., Maselli, F., Moriondo, M., Gioli, B., Toscano, P., Zaldei, A., Bindi, M., 2013. Simulation of olive grove gross primary production by the combination of ground and multi-sensor satellite data. Int. J. Appl. Earth Obs. Geoinf. 23, 29–36. https://doi.org/10.1016/j.jag.2012.11.006.

Bye, I.J., North, P.R.J., Los, S.O., Kljun, N., Rosette, J.A.B., Hopkinson, C., Chasmer, L., Mahoney, C., 2017. Estimating forest canopy parameters from satellite waveform LiDAR by inversion of the FLIGHT three-dimensional radiative transfer model. Remote Sens. Environ. 188, 177–189. https://doi.org/10.1016/j.rse.2016.10.048.

Castillo, J.A.A., Apan, A.A., Maraseni, T.N., Salmo, S.G., 2017. Estimation and mapping of above-ground biomass of mangrove forests and their replacement land uses in the Philippines using Sentinel imagery. ISPRS J. Photogrammetry Remote Sens. 134, 70–85. https://doi.org/10.1016/j.isprsjprs.2017.10.016.

Chen, J.M., 1996. Evaluation of vegetation indices and a modified Simple ratio for boreal applications. Can. J. Remote Sens. 22, 229–242. https://doi.org/10.1080/07038992.1996.10855178.

Cleveland, W.S., Grosse, E., Shyu, W.M., 1992. Local regression models. Statistical models in S 2, 309–376.

Commission Implementing Decision (EU) 2018/927 of 27, 2018. June 2018 amending Implementing Decision (EU) 2015/789 as regards measures to prevent the introduction into and the spread within the Union of Xylella fastidiosa (Wells et al.) (notified under document C(2018) 3972). OJ L.

Dash, J., Curran, P.J., 2007. Evaluation of the MERIS terrestrial chlorophyll index (MTCI). Adv. Space Res. 39, 100–104. https://doi.org/10.1016/j.asr.2006.02.034.

Delegido, J., Verrelst, J., Alonso, L., Moreno, J., 2011. Evaluation of sentinel-2 red-edge bands for empirical estimation of green LAI and chlorophyll content. Sensors 11, 7063–7081. https://doi.org/10.3390/s110707063.

EFSA, 2018. Updated pest categorisation of Xylella fastidiosa. EFSA Journal 16, e05357. https://doi.org/10.2903/j.efsa.2018.5357.

EPPO, 2019. First Report of Xylella Fastidiosa in Israel. EPPO Reporting Service No. 6, Global Database. [WWW Document]. URL. https://gd.eppo.int/reporting/article-6551 accessed 9.16.19.

Fang, X., Zhu, Q., Ren, L., Chen, H., Wang, K., Peng, C., 2018. Large-scale detection of vegetation dynamics and their potential drivers using MODIS images and BFAST: a case study in Quebec, Canada. Remote Sens. Environ. 206, 391–402. https://doi.org/10.1016/j.rse.2017.11.017.

Feret, J.-B., Gitelson, A., Noble, S.D., Jacquemoud, S., 2017. PROSPECT-d: towards modeling leaf optical properties through a complete lifecycle. Remote Sens. Environ. 193, 204–215. https://doi.org/10.1016/j.rse.2017.03.004.

Forkuor, G., Dimobe, K., Serme, I., Tondoh, J.E., 2018. Landsat-8 vs. Sentinel-2: examining the added value of sentinel-2's red-edge bands to land-use and land-cover mapping in Burkina Faso. GIScience Remote Sens. 55, 331–354. https://doi.org/10.1080/15481603.2017.1370169.

Frampton, William James, Dash, J., Watmough, G., Milton, E.J., 2013a. Evaluating the capabilities of Sentinel-2 for quantitative estimation of biophysical variables in vegetation. ISPRS J. Photogrammetry Remote Sens. 82, 83–92. https://doi.org/10.1016/j.isprsjprs.2013.04.007.

Frampton, W.J., Dash, J., Watmough, Gary R., Milton, E.J., 2013b. Evaluating the Capabilities of Sentinel-2 for Quantitative Estimation of Biophysical Variables in Vegetation ISPRS Journal of Photogrammetry and Remote Sensing, vol. 82. pp. 83–92. https://doi.org/10.1016/j.isprsjprs.2013.04.007.

Fuente, B. de la, Saura, S., Beck, P.S.A., 2018. Predicting the spread of an invasive tree pest: the pine wood nematode in Southern Europe. J. Appl. Ecol. 55, 2374–2385. https://doi.org/10.1111/1365-2664.13177.

Gamon, J.A., Surfus, J.S., 1999. Assessing leaf pigment content and activity with a reflectometer. New Phytol. 143, 105–117. https://doi.org/10.1046/j.1469-8137.1999.00424.x.

Gastellu-Etchegorry, J.P., Demarez, V., Pinel, V., Zagolski, F., 1996. Modeling radiative transfer in heterogeneous 3-D vegetation canopies. Remote Sens. Environ. 58, 131–156. https://doi.org/10.1016/0034-4257(95)00253-7.

Gillespie, T.W., Ostermann-Kelm, S., Dong, C., Willis, K.S., Okin, G.S., MacDonald, G.M., 2018. Monitoring changes of NDVI in protected areas of southern California. Ecol. Indicat. 88, 485–494. https://doi.org/10.1016/j.ecolind.2018.01.031.

Girelli, C.R., Coco, L.D., Scortichini, M., Petriccione, M., Zampella, L., Mastrobuoni, F., Cesari, G., Bertaccini, A., D'Amico, G., Contaldo, N., Migoni, D., Fanizzi, F.P., 2017. Xylella fastidiosa and olive quick decline syndrome (CoDiRO) in Salento (southern Italy): a chemometric 1H NMR-based preliminary study on Ogliarola salentina and Cellina di Nardò cultivars. Chem. Biol. Technol. Agric. 4, 25. https://doi.org/10.1186/s40538-017-0107-7.

Gitelson, A.A., Kaufman, Y.J., Merzlyak, M.N., 1996. Use of a green channel in remote sensing of global vegetation from EOS-MODIS. Remote Sens. Environ. 58, 289–298. https://doi.org/10.1016/S0034-4257(96)00072-7.

Gómez Calero, J.A., Zarco-Tejada, P.J., García-Morillo, J., Gama, J., Soriano, M.A., 2011. Determining biophysical parameters for olive trees using CASI-airborne and QuickBird-satellite imagery. https://doi.org/10.2134/agronj2010.0449.

Gueymard, C., 1995. SMARTS2: a Simple Model of the Atmospheric Radiative Transfer of Sunshine: Algorithms and Performance Assessment. Florida Solar Energy Center Cocoa, FL.

Gueymard, C.A., 2001. Parameterized transmittance model for direct beam and circumsolar spectral irradiance. Sol. Energy 71, 325–346. https://doi.org/10.1016/S0038-092X(01)00054-8.

Haboudane, D., Miller, J.R., Pattey, E., Zarco-Tejada, P.J., Strachan, I.B., 2004. Hyperspectral vegetation indices and novel algorithms for predicting green LAI of crop canopies: modeling and validation in the context of precision agriculture. Remote Sens. Environ. 90, 337–352. https://doi.org/10.1016/j.rse.2003.12.013.

Haboudane, D., Miller, J.R., Tremblay, N., Zarco-Tejada, P.J., Dextraze, L., 2002. Integrated narrow-band vegetation indices for prediction of crop chlorophyll content for application to precision agriculture. Remote Sens. Environ. 81, 416–426. https://doi.org/10.1016/S0034-4257(02)00018-4.

Haboudane, D., Tremblay, N., Miller, J.R., Vigneault, P., 2008. Remote estimation of crop chlorophyll content using spectral indices derived from hyperspectral data. IEEE Trans. Geosci. Remote Sens. 46, 423–437. https://doi.org/10.1109/TGRS.2007.904836.

Harrower, M., Brewer, C.A., 2003. ColorBrewer. org: an online tool for selecting colour schemes for maps. Cartogr. J. 40, 27–37.

Hay, S.I., Tatem, A.J., Graham, A.J., Goetz, S.J., Rogers, D.J., 2006. Global environmental data for mapping infectious disease distribution. Adv. Parasitol. 62, 37–77. https://doi.org/10.1016/S0065-308X(05)62002-7.

Haynes, W., 2013. Bonferroni Correction, in: Encyclopedia of Systems Biology. Springer, New York, NY. https://doi.org/10.1007/978-1-4419-9863-7_1213. 154–154.

Hernández-Clemente, R., Navarro-Cerrillo, R.M., Ramírez, F.J.R., Hornero, A., Zarco-Tejada, P.J., 2014. A novel methodology to estimate single-tree biophysical parameters from 3D digital imagery compared to aerial laser scanner data. Remote Sens. 6, 11627–11648. https://doi.org/10.3390/rs61111627.

Hernández-Clemente, R., Navarro-Cerrillo, R.M., Suárez, L., Morales, F., Zarco-Tejada, P.J., 2011. Assessing structural effects on PRI for stress detection in conifer forests. Remote Sens. Environ. 115, 2360–2375. https://doi.org/10.1016/j.rse.2011.04.036.

Hernández-Clemente, R., Navarro-Cerrillo, R.M., Zarco-Tejada, P.J., 2012. Carotenoid content estimation in a heterogeneous conifer forest using narrow-band indices and PROSPECT + DART simulations. Remote Sens. Environ. 127, 298–315. https://doi.org/10.1016/j.rse.2012.09.014.

Hernández-Clemente, R., North, P.R.J., Hornero, A., Zarco-Tejada, P.J., 2017. Assessing the effects of forest health on sun-induced chlorophyll fluorescence using the FluorFLIGHT 3-D radiative transfer model to account for forest structure. Remote Sens. Environ. 193, 165–179. https://doi.org/10.1016/j.rse.2017.02.012.

Herrmann, I., Karnieli, A., Bonfil, D.J., Cohen, Y., Alchanatis, V., 2010. SWIR-based spectral indices for assessing nitrogen content in potato fields. Int. J. Remote Sens. 31, 5127–5143. https://doi.org/10.1080/01431160903283892.
Herrmann, I., Pimstein, A., Karnieli, A., Cohen, Y., Alchanatis, V., Bonfil, D.J., 2011. LAI assessment of wheat and potato crops by VENμS and Sentinel-2 bands. Remote Sens. Environ. 115, 2141–2151. https://doi.org/10.1016/j.rse.2011.04.018.
Hill, M.J., 2013. Vegetation index suites as indicators of vegetation state in grassland and savanna: an analysis with simulated SENTINEL 2 data for a North American transect. Remote Sens. Environ. 137, 94–111. https://doi.org/10.1016/j.rse.2013.06.004.
Horsfall, J.G., Cowling, E.B., 1978. Pathometry: the measurement of plant disease. Plant Disease: an Advanced Treatise 2, 120–136.
Huete, A., Justice, C., Liu, H., 1994. Development of vegetation and soil indices for MODIS-EOS. Remote Sens. Environ. 49, 224–234. https://doi.org/10.1016/0034-4257(94)90018-3.
Huete, A.R., 1988. A soil-adjusted vegetation index (SAVI). Remote Sens. Environ. 25, 295–309. https://doi.org/10.1016/0034-4257(88)90106-X.
Huete, A.R., Jackson, R.D., Post, D.F., 1985. Spectral response of a plant canopy with different soil backgrounds. Remote Sens. Environ. 17, 37–53. https://doi.org/10.1016/0034-4257(85)90111-7.
InnovaPuglia Spa - Servizio Territorio e Ambiente, 2013. Uso del Suolo. [WWW Document]. URL. http://www.dataset.puglia.it/dataset/uso-del-suolo-2011-uds accessed 9.2.18.
Karnieli, A., Kaufman, Y.J., Remer, L., Wald, A., 2001. AFRI — aerosol free vegetation index. Remote Sens. Environ. 77, 10–21. https://doi.org/10.1016/S0034-4257(01)00190-0.
Kaufman, Y.J., Tanre, D., 1992a. Atmospherically resistant vegetation index (ARVI) for EOS-MODIS. IEEE Trans. Geosci. Remote Sens. 30, 261–270. https://doi.org/10.1109/36.134076.
Kaufman, Y.J., Tanre, D., 1992b. Atmospherically resistant vegetation index (ARVI) for EOS-MODIS. IEEE Trans. Geosci. Remote Sens. 30, 261–270. https://doi.org/10.1109/36.134076.
Korhonen, L., Korpela, I., Heiskanen, J., Maltamo, M., 2011. Airborne discrete-return LIDAR data in the estimation of vertical canopy cover, angular canopy closure and leaf area index. Remote Sens. Environ. 115, 1065–1080. https://doi.org/10.1016/j.rse.2010.12.011.
Lange, M., Dechant, B., Rebmann, C., Vohland, M., Cuntz, M., Doktor, D., 2017. Validating MODIS and sentinel-2 NDVI products at a temperate deciduous forest site using two independent ground-based sensors. Sensors 8, 11–17. https://doi.org/10.3390/s17081855.
Luvisi, A., Aprile, A., Sabella, E., Vergine, M., Nicolì, F., Nutricati, E., Miceli, A., Negro, C., Bellis, L.D., 2017. Xylella fastidiosa subsp. pauca (CoDiRO strain) infection in four olive ( Olea europaea L.) cultivars: profile of phenolic compounds in leaves and progression of leaf scorch symptoms. Phytopathol. Mediterr. 56https://doi.org/10.14601/Phytopathol_Mediterr-20578. 259-273–273.
Martín, A., Zarco-Tejada, P.J., González, M.R., Berjón, A., 2007. Using Hyperspectral Remote Sensing to Map Grape Quality in “Tempranillo” Vineyards Affected by Iron Deficiency Chlorosis.
Meggio, F., Zarco-Tejada, P.J., Miller, J.R., Martín, A., González, M.R., Berjón, A., 2008. Row Orientation and Viewing Geometry Effects on Row-Structured Crops for Chlorophyll Content Estimation.
Montandon, L.M., 2009. The Impact of Soil Properties on Soil NDVI and the Quantification of the Green Vegetation Fraction (Ph.D.). University of Colorado at Boulder, United States – Colorado.
Mura, M., Bottalico, F., Giannetti, F., Bertani, R., Giannini, R., Mancini, M., Orlandini, S., Travaglini, D., Chirici, G., 2018. Exploiting the capabilities of the Sentinel-2 multi spectral instrument for predicting growing stock volume in forest ecosystems. Int. J. Appl. Earth Obs. Geoinf. 66, 126–134. https://doi.org/10.1016/j.jag.2017.11.013.
Myneni, R.B., Marshak, A., Knyazikhin, Y., Asrar, G., 1991. Discrete Ordinates Method for Photon Transport in Leaf Canopies, in: Photon-Vegetation Interactions. Springer, Berlin, Heidelberg, pp. 45–109. https://doi.org/10.1007/978-3-642-75389-3_3.
Niblack, W., 1986. An Introduction to Digital Image Processing, First English Edition edition. Prentice Hall, Englewood Cliffs, N.J.
Noori, O., Panda, S.S., 2016. Site-specific management of common olive: remote sensing, geospatial, and advanced image processing applications. Comput. Electron. Agric. 127, 680–689. https://doi.org/10.1016/j.compag.2016.07.031.
North, P.R.J., 1996. Three-dimensional forest light interaction model using a Monte Carlo method. IEEE Trans. Geosci. Remote Sens. 34, 946–956. https://doi.org/10.1109/36.508411.
Nutter, F.W., Esker, P.D., Netto, R.A.C., 2006. Disease assessment concepts and the advancements made in improving the accuracy and precision of plant disease data. Eur. J. Plant Pathol. 115, 95–103. https://doi.org/10.1007/s10658-005-1230-z.
Pearson, R.L., Miller, L.D., 1972. Remote mapping of standing crop biomass for estimation of the productivity of the shortgrass prairie. Presented at the Remote Sensing of Environment VIII, 1355.
Peltzer, D.A., Köchy, M., 2001. Competitive effects of grasses and woody plants in mixed-grass prairie. J. Ecol. 89, 519–527.
Pinty, B., Verstraete, M.M., 1992. GEMI: a non-linear index to monitor global vegetation from satellites. Vegetatio 101, 15–20. https://doi.org/10.1007/BF00031911.
Qi, J., Chehbouni, A., Huete, A.R., Kerr, Y.H., Sorooshian, S., 1994. A modified soil adjusted vegetation index. Remote Sens. Environ. 48, 119–126. https://doi.org/10.1016/0034-4257(94)90134-1.
Rahimzadeh-Bajgiran, P., Weiskittel, A.R., Kneeshaw, D., MacLean, D.A., 2018. Detection of annual spruce budworm defoliation and severity classification using Landsat imagery. Forests 9, 357. https://doi.org/10.3390/f9060357.
Richardson, A.J., Wiegand, C.L., 1977. Distinguishing vegetation from soil background information. [by gray mapping of Landsat MSS data]. Photogramm. Eng. Remote Sens. 43, 1541–1552.
Richter, R., Wang, X., Bachmann, M., Schläpfer, D., 2011. Correction of cirrus effects in sentinel-2 type of imagery. Int. J. Remote Sens. 32, 2931–2941. https://doi.org/10.1080/01431161.2010.520346.
Rivera, J.P., Verrelst, J., Gómez-Dans, J., Muñoz-Marí, J., Moreno, J., Camps-Valls, G., 2015. An emulator toolbox to approximate radiative transfer models with statistical learning. Remote Sens. 7, 9347–9370. https://doi.org/10.3390/rs70709347.
Rondeaux, G., Steven, M., Baret, F., 1996. Optimization of soil-adjusted vegetation indices. Remote Sens. Environ. 55, 95–107. https://doi.org/10.1016/0034-4257(95)00186-7.
Roujean, J.-L., Breon, F.-M., 1995. Estimating PAR absorbed by vegetation from bidirectional reflectance measurements. Remote Sens. Environ. 51, 375–384. https://doi.org/10.1016/0034-4257(94)00114-3.
Rouse Jr., J.W., Haas, R.H., Schell, J.A., Deering, D.W., 1974. Monitoring vegetation systems in the great plains with erts. 351. NASA Special Publication, pp. 309.
Saponari, M., Boscia, D., Altamura, G., Loconsole, G., Zicca, S., D'Attoma, G., Morelli, M., Palmisano, F., Saponari, A., Tavano, D., Savino, V.N., Dongiovanni, C., Martelli, G.P., 2017. Isolation and pathogenicity of Xylella fastidiosa associated to the olive quick decline syndrome in southern Italy. Sci. Rep. 7, 17723. https://doi.org/10.1038/s41598-017-17957-z.
Sauvola, J., Pietikäinen, M., 2000. Pietikainen, M.: adaptive document image binarization. Pattern Recognit. 33, 225–236. https://doi.org/10.1016/S0031-3203(99)00055-2.
Seem, R.C., 1984. Disease incidence and severity relationships. Annu. Rev. Phytopathol. 22, 133–150. https://doi.org/10.1146/annurev.py.22.090184.001025.
Sibbett, G.S., Ferguson, L., 2005. Olive Production Manual. UCANR Publications.
Sisterson, M.S., Thammiraju, S.R., Lynn-Patterson, K., Groves, R.L., Daane, K.M., 2010. Epidemiology of diseases caused by Xylella fastidiosa in California: evaluation of alfalfa as a source of vectors and inocula. Plant Dis. 94, 827–834. https://doi.org/10.1094/PDIS-94-7-0827.
Strona, G., Carstens, C.J., Beck, P.S.A., 2017. Network analysis reveals why Xylella fastidiosa will persist in Europe. Sci. Rep. 7, 71. https://doi.org/10.1038/s41598-017-00077-z.
Verhoef, W., 1984. Light scattering by leaf layers with application to canopy reflectance modeling: the SAIL model. Remote Sens. Environ. 16, 125–141. https://doi.org/10.1016/0034-4257(84)90057-9.
White, S.M., Bullock, J.M., Hooftman, D.A.P., Chapman, D.S., 2017. Modelling the spread and control of Xylella fastidiosa in the early stages of invasion in Apulia, Italy. Biol. Invasions 19, 1825–1837. https://doi.org/10.1007/s10530-017-1393-5.
Whyte, A., Ferentinos, K.P., Petropoulos, G.P., 2018. A new synergistic approach for monitoring wetlands using Sentinels -1 and 2 data with object-based machine learning algorithms. Environ. Model. Softw 104, 40–54. https://doi.org/10.1016/j.envsoft.2018.01.023.
Yáñez-Rausell, L., Malenovský, Z., Rautiainen, M., Clevers, J.G.P.W., Lukeš, P., Hanuš, J., Schaepman, M.E., 2015. Estimation of spruce needle-leaf chlorophyll content based on DART and PARAS canopy reflectance models. IEEE Journal of Selected Topics in Applied Earth Observations and Remote Sensing 8, 1534–1544. https://doi.org/10.1109/JSTARS.2015.2400418.
Yang, W., Kobayashi, H., Suzuki, R., Nasahara, K.N., 2014. A Simple method for retrieving understory NDVI in sparse needleleaf forests in Alaska using MODIS BRDF data. Remote Sens. 6, 11936–11955. https://doi.org/10.3390/rs61211936.
Zarco-Tejada, P.J., Camino, C., Beck, P.S.A., Calderon, R., Hornero, A., Hernández-Clemente, R., Kattenborn, T., Montes-Borrego, M., Susca, L., Morelli, M., Gonzalez-Dugo, V., North, P.R.J., Landa, B.B., Boscia, D., Saponari, M., Navas-Cortes, J.A., 2018. Previsual symptoms of Xylella fastidiosa infection revealed in spectral plant-trait alterations. Nature Plants 4, 432–439. https://doi.org/10.1038/s41477-018-0189-7.
Zarco-Tejada, P.J., González-Dugo, M.V., Fereres, E., 2016. Seasonal stability of chlorophyll fluorescence quantified from airborne hyperspectral imagery as an indicator of net photosynthesis in the context of precision agriculture. Remote Sens. Environ. 179, 89–103. https://doi.org/10.1016/j.rse.2016.03.024.
Zarco-Tejada, P.J., Hornero, A., Beck, P.S.A., Kattenborn, T., Kempeneers, P., Hernández-Clemente, R., 2019. Chlorophyll content estimation in an open-canopy conifer forest with Sentinel-2A and hyperspectral imagery in the context of forest decline. Remote Sens. Environ. 223, 320–335. https://doi.org/10.1016/j.rse.2019.01.031.
Zarco-Tejada, P.J., Hornero, A., Hernández-Clemente, R., Beck, P.S.A., 2018b. Understanding the temporal dimension of the red-edge spectral region for forest decline detection using high-resolution hyperspectral and Sentinel-2a imagery. ISPRS J. Photogrammetry Remote Sens. 137, 134–148. https://doi.org/10.1016/j.isprsjprs.2018.01.017.
Zarco-Tejada, P.J., Miller, J.R., Mohammed, G.H., Noland, T.L., Sampson, P.H., 2001. Estimation of chlorophyll fluorescence under natural illumination from hyperspectral data. Int. J. Appl. Earth Obs. Geoinf. 3, 321–327. https://doi.org/10.1016/S0303-2434(01)85039-X.
Zarco-Tejada, P.J., Morales, A., Testi, L., Villalobos, F.J., 2013. Spatio-temporal patterns of chlorophyll fluorescence and physiological and structural indices acquired from hyperspectral imagery as compared with carbon fluxes measured with eddy covariance. Remote Sens. Environ. 133, 102–115. https://doi.org/10.1016/j.rse.2013.02.003.
Zhang, Y., Chen, J.M., Miller, J.R., Noland, T.L., 2008. Leaf chlorophyll content retrieval from airborne hyperspectral remote sensing imagery. Remote Sens. Environ. 112, 3234–3247. https://doi.org/10.1016/j.rse.2008.04.005.
Zurita-Milla, R., Laurent, V.C.E., van Gijsel, J.A.E., 2015. Visualizing the ill-posedness of the inversion of a canopy radiative transfer model: a case study for Sentinel-2. International Journal of Applied Earth Observation and Geoinformation, Special Issue on “Advances in remote sensing of vegetation function and traits” 43, 7–18. https://doi.org/10.1016/j.jag.2015.02.003.